5-11-2023

Atmospheric Impacts from the 2010 Deepwater Horizon Oil Spill

Charles Philip Johnson
Louisiana State University and Agricultural and Mechanical College

ATMOSPHERIC IMPACTS FROM THE 2010 *DEEPWATER HORIZON* OIL SPILL

A Thesis

Submitted to the Graduate Faculty of the
Louisiana State University and
Agricultural and Mechanical College
in partial fulfillment of the
requirements of the degree of
Master of Science

in

The Department of Oceanography and Coastal Sciences

by
Charles Philip Johnson
B.S., Mississippi State University, 2020
August 2023

Table of Contents

List of Tables

List of Figures

Abstract

Although the ecological devastations induced by an oil spill are well studied, the hydrometeorological impacts from a long-term slick have gone unnoticed. The ocean-surface alterations stemming from the lasting oil footprint increase solar radiation absorption which in turn alters the atmospheric sea level pressure (SLP) and moisture gradients and wind speeds thereby influencing precipitation surrounding the oil spill. Revealing the potential impacts from these could better aid in the safety of crews cleaning spills and provide a better understanding of how humans alter the landscape. This thesis examines the changes in local hydrometeorology brought on by the 20 April – 19 September 2010 *Deepwater Horizon* (DWH) oil spill in the northern Gulf of Mexico (GOM). Five Weather Research and Forecasting (WRF) 4.2 simulations are utilized to establish potential impacts on pressure, wind, cloud fraction, and precipitation to ERA5 Reanalysis data with and without increased sea surface temperatures (SSTs) from the oil slick footprint.

During the time period of the simulations, compared to the control, the experimental scenarios suggest an increase in 2-m dewpoint temperatures and a decrease in SLP from the increased SSTs and implementation of the oil footprint. Additionally, the experimental scenarios display a ten-or-more percent increase in mid- to high-level cloud fractions compared to the control and a ten-or-more percent decrease in low-level cloud fractions. Roughly 300mm of greater experimental precipitation accumulation occurred across the portion of the GOM within the inner domain of the spill, implying that the alterations made within the scenarios influence the spatial and temporal patterns of precipitation.

Chapter 1. Introduction

Oil spills are a persistent problem for marine communities, and while the impacts on ocean ecology have been studied extensively (e.g., EPA 2022), the atmospheric effects from oil slicks have yet to be examined with the same vigor. These environmental disasters can last months and span areas of thousands of square kilometers. The possibility of these large oil areas affecting the surface energy budget seems likely as a darkening of the ocean surface would lead to increased absorption of incoming solar radiation while perturbing evaporation rates and raising surface temperatures. An area of increased temperature compared to its surrounding environment could result in the formation of a thermal low, causing clouds and thunderstorms, similar to the urban heat island effect (Han et al. 2014). This research will shed light on this under-studied aspect of oil spills as well as provide knowledge for those in the clean-up process and potential effects and provide a basis for further research into atmospheric and ocean circulation and stratification impacts.

Statistically, since the 1970s, the number of oil spills has been on the decline globally (International Tanker Owners Pollution Federation Limited 2022). However, the Bureau of Safety and Environmental Enforcement (BSEE) oil spill archive shows that the oil spills are likely to continue into the foreseeable future. Each spill between the 1960s and 2013 is marked as being caused by equipment failure, human error, or extreme weather (BSEE 2013). Errors and negligence are impossible to remove fully, and natural disasters are a phenomenon that has forever plagued humanity and are only likely to increase in severity moving forward (IPCC AR6 2022). As long as humanity uses oil, accidents will occur eventually. It is therefore important to understand the short and long-term environmental impacts of these disasters. While the focus is typically on the marine environment, there is beneficial knowledge in understanding an oil spill's

ability to heat the ocean surface to the point of altering convection patterns. This also further applies to worker safety during clean-ups as an increase in convection may lead to greater cloud and thunderstorm formation as well as lightning frequency.

The aim of this study is to use ERA5 Reanalysis data over the GOM from May – August 2010 to examine and SSTs as well as atmospheric metrics such as precipitation and cloud generation to answer the question: Can the presence of oil impact local hydrometeorology in the Gulf of Mexico? It is hypothesized that the *Deepwater Horizon* oil spill resulted in above-average cloud and thunderstorm development within the oil slick footprint. The size, duration, and timing of the 2010 *Deepwater Horizon* oil spill provides a unique opportunity to study an unexamined environmental phenomenon.

Chapter 2 contains an overview of the *Deepwater Horizon* oil spill, as well as studies on remote sensing of oil slicks and SST, and oil slick interactions with SSTs. Chapter 3 details the research design and methods and a summary of the synoptic scale factors influencing the summer of 2010. Additionally, Chapter 3 will include the specifications for the control and four experimental Weather Research and Forecasting (WRF) simulations. In Chapter 4, the model validation is conducted and discusses how the model alterations impact sea level pressure, wind speed, and cloud activity and how those variables impact precipitation. Chapter 5 draws connections between these variables and how these relate to the summer-wide study duration. Chapter 6 aggregates the atmospheric impacts from the *Deepwater Horizon* oil spill as well as the potential for future studies related to this type of modeling.

Chapter 2. Literature Review

To determine the atmospheric impacts of the 2010 *Deepwater Horizon* spill, the location, duration, and context of clean-up must be established. This chapter will provide information on the following: [1] the oil spill event and scope, [2] remote sensing techniques for identifying oil slicks and their motion, [3] remote sensing techniques for assessing sea surface temperature (SST), [4] thermodynamic influences of oil on ocean temperatures, and [5] possible atmospheric impacts using an analogous environmental situation, the urban heat island.

2.1. Deepwater Horizon

On 20 April 2010, the oil platform *Deepwater Horizon* suffered a backup of natural gases, resulting in an explosion that killed 11 crew members and injured 17 more. Two days later, on 22 April, the rig capsized and sank while the blowout preventer beneath the surface failed, resulting in oil and natural gas flowing freely from the Macondo oil well for 87 days before it was finally capped on 15 July (McNutt et al. 2012, Joye 2015). The volume of oil discharged across this period is uncertain as it was not feasible to measure how much gas and oil were coming directly from the pipe. Initially, estimates were quite low with the British Petroleum Company (BP) stating that the flow was only at a rate of roughly 1000 barrels per day (MacDonald 2010, Bothun 2019). However, it was eventually judged that flow rates were much greater. Many methods were implemented, including airborne and satellite estimations, chemical measurements, acoustic measurements, and modeling. The consensus is that the rate was between 50,000 to 70,000 barrels per day with a total of over 210 million gallons of oil and 250,000 metric tons of natural gas being released (Crone & Tolstoy 2010, Camilli et al. 2011, Olascoaga & Haller 2012, Ryerson et al. 2012, Joye 2015, MacDonald et al. 2015). This disaster forced months-long shutdowns of many coastal industries and resulted in a loss of billions of

dollars across coastal communities and in cleanup efforts (Cohen 2010, Court et al. 2019). By the start of June, up to 229,271 km² of federal waters had been shut down due to oil impacts (Ylitalo et al. 2012). Composite images of synthetic aperture radar (SAR) data showed that between April and August oil covered an area of 149,000 km² (MacDonald et al. 2015). This means that 9.31% of the Gulf of Mexico, with an area of roughly 1,600,095 square kilometers, was covered in oil across the five-month period.

2.2. Remote Sensing of Oil Spills

Remote sensing of oil spills has been practiced for decades and especially since the late 1990s (Xue et al. 2008). It allows for a wide-scale viewing approach as well as rapid updates. Remote sensing can even allow the detection of the thickness of an oil patch (Tseng & Chiu 1994). The most common methods of remote sensing of oil are at visible, infrared, ultraviolet, or radio wavelengths. The visible range of the electromagnetic spectrum extends from about 400 to 700nm and for a long time was the most popular wavelength band for identifying oil patches in oceans (Fingas & Brown 1997). For the Exxon Valdez oil spill of 1989, the use of visible remote sensing data through flyovers of the Alaskan coastline was instrumental in cleanup efforts (Taft et al. 1995). Visible satellite data are used by comparing the glint or sheen of the oil patch to the surrounding water (Fingas & Brown 1997, 2017). The problem with relying on this wavelength band is that instruments recording visible wavelength bands are passive sensors. As such, they rely solely on incoming radiation from the Sun reflecting off the Earth into the sensor's field of view. It is therefore impossible to use these sensors at night or when cloud cover is substantial. Moreover, the glinting of the Sun off the ocean surface could cause errors when deducing oil locations (Fingas & Brown 2014).

These problems can be somewhat alleviated through techniques such as polarization. The basic process of polarization filters out either the vertical or horizontal portion of the wavelength from incoming light, allowing optical remote sensors to highlight different features within the ocean-scape surface (Tyo et al. 2006, Shen et al. 2011). Polarization is still cumbersome to use as it relies on precise satellite location and angle of reflecting light as well as suitable ocean conditions. Strong winds minimize effectiveness, as light from moving water is problematic (Shen et al., 2011). While valuable, visible data has substantial limitations for oil spill assessment.

Infrared sensors are another method of identifying oil spills, with most thermal infrared region (TIR) instruments sensing a wavelength range between 8 and 14 μm. Within this region, oil is unique when backdropped with water. Its smaller heat capacity than water coupled with a wide diurnal temperature range makes it readily apparent in the TIR band, especially during afternoons when it can absorb more heat than the surrounding water (Samberg 2005). Conversely during the nighttime, the oil cools rapidly, making it appear cooler compared to the ocean; however, these properties also mean that different water masses or frontal systems within the ocean could be misinterpreted as oil slicks (Samberg 2005). TIR instruments can also help determine the thickness of the oil spill. Pockets with thicker quantities of oil absorb more incoming solar radiation than thinner patches so thicker areas appear warmer, while thinner regions appear cooler. Very thin areas of oil are impossible to detect with TIR-based imagery and areas of high emulsion through wave agitation are similarly undetectable using TIR-based imagery (Salisbury 1993, Fingas & Brown 1997, Jha et al. 2008). TIR could also be used to determine the location from which oil is erupting. Xing et al. (2015) used the *Deepwater Horizon* oil spill to study TIR brightness temperature and found that there were cold patches of

oil surrounding the oil rig and warm patches farther away, likely because of the oil near the ocean floor exchanging heat with the surrounding environment before upwelling and appearing cooler than the surface oil or water.

Ultraviolet wavelength bands are also used to detect oil spills due to the highly reflective nature of ultraviolet light on oil. The reflectivity of oil in this range is 1.02 to only 0.722 (unitless) for water making it a great candidate for viewing (Goodman 1994) even, thin layers of oil. It can view oil patches less than 0.1 μm thick due to it being a measure of reflectivity as opposed to the TIR's emissivity (Grüner et al. 1991). This proves to be a double-edged sword as reflectivity is only viewable on the ocean surface during the day and ultraviolet sensors cannot determine thickness (Grüner et al. 1991, Goodman 1994, Fingas & Brown 1997, Jha et al. 2008). Moreover, ultraviolet sensors are passive, reflective-based devices making them highly sensitive to sun glint and ocean topography. Suo et al. (2021) reported on the new Chinese satellite Haiyang-1C to determine a satellite's capability to use the ultraviolet spectrum to determine oil slicks, finding that the angle of the satellite plays a major role in determining oil reflectance. They concluded that determining oil solely through ultraviolet bands is ineffective but could be used in conjunction with TIR to compensate for each band's weaknesses (Fingas & Brown 2013, Suo et al. 2021).

The most common choices of radar imagery with oil presently are SAR or Side-Looking Airborne Radar (SLAR). SLAR uses an extended radar antenna whereas SAR uses the motion of an aircraft to create the same effect but with better resolution and higher accuracy; hence the name *synthetic* aperture radar (Fingas & Brown 1997, Doerry & Dickey 2004). Within the scope of radar bands, it has been found that X (3.75 – 2.4 cm wavelength), C (7.5 – 3.75 cm wavelength), and L (30 – 15 cm wavelength) bands are adept at spotting oil slicks; however, X

functions the best as the difference between backscattering and the ocean is most apparent at this frequency (Yang et al. 2009). These methods work due to a dampening of capillary waves by oil on top of the ocean surface. Capillary waves are tiny waves often seen as ripples caused by wind or another disturbing force that is restored to balance via water tension. Capillary waves are highly reflective of radio waves so when oil settles atop the water, radar imagery can capture oil due to the contrasting nature of the reflective surrounding marine environment and dampened oil (Gade et al. 1998, Wisman et al. 1998). In SAR or SLAR imagery, the normally bright, reflective ocean surface would appear dark when oil is on top. Taking it a step further, this means that anything that would dampen these waves would appear dark. Nevertheless, many ocean phenomena such as seaweed patches, fish sperm, internal waves, and freshwater plumes can create false positives within the radar imagery (Brekke & Solberg 2005, Espedal 1999, Walker et al. 2011, Fingas & Brown 2014). Wind can be another distorting factor for SAR imagery. Ideally, the wind would be between 5 – 6 m s^{-1} as this provides enough force to create capillary waves but not so much that the surface would become too choppy to view (Jones 2001). The full range of detection is between roughly 2 – 12 m s^{-1}, with emphasis on the 4 – 7 m s^{-1} range being important to recognize the wind patterns for identifying an object as (Jones 2001). They could be used quite well in conjunction with the other detection methods as SAR imagery can be used during the nighttime and inclement weather complementing the higher resolutions of infrared imagery and visible (Good et al. 2011).

2.3. Remote Sensing of SSTs

SSTs are essential to understanding global heat transport and air-sea interactions. It was only in the late 1970s, however, that technology was readily available to study SSTs outside of difficult-to-obtain *in-situ* data (Minnet et al. 2019). With the launch of infrared satellites

followed by the rapid improvement of instruments to close the error gap between *in-situ* measurements, a new era of global SST study could begin. This allowed higher-resolution images and a way to study global currents on a broad scale (Legeckis 1979, McClain et al. 1985). Satellite sensors rely on a radiometer measuring the amount of infrared energy being emitted from an object, or in this case a body of water. Because historically *in-situ* SST data has been measured through floats, buoys, and ships, the term "bulk SSTs" (Emery et al. 2001) refers to values between 0.5 and 5 m below the actual surface. Because the satellite can only measure roughly the top 10 μm of the ocean surface, satellites must estimate the bulk SST. Clouds pose a problem for infrared (IR) SSTs because IR sensors cannot penetrate clouds as effectively as microwave imagery can. This means that if a cloud is present, it must be either edited out through composite imagery or masked through algorithms. Composite imagery is useful for capturing cloud-free areas using multiple sweeps across the viewing (Haines et al. 2007). This method is imperfect as it cannot always be guaranteed that the cloud will move in time or that there will be another sweep of the area promptly. Cloud masking does not remove clouds from the images seen as well as composite imaging does, but it indicates a cloud is obfuscating the view instead of falsely suggesting a cold spot. While many algorithms for cloud masking exist, the basic idea is that pixels are compared to their surrounding ones and depending on the contrast the algorithm decides whether to mask it (Frey et al. 2008). This technique is simple and effective, but it also means that areas of high contrast, such as along the coast and especially strong ocean fronts can be mistaken for clouds and subsequently masked.

2.4. Oil Effect on Ocean Surface and SSTs

At the initiation of an oil spill, SSTs can affect the spreading of oil. While there are few studies on SSTs as they relate to oil, Samra et al. (2021) found that SSTs were important to oil

viscosity. Their study of coastal Egypt revealed that during winter days offshore waters were warmer and would disperse oil faster than coastal regions. The opposite is true for summer during the day when the coastal water is warmer than offshore and oil would disperse more rapidly along the coast. At night, in both the winter and summer the coast is warmer than the offshore, resulting in oil dispersing faster along the coast (Samra et al. 2021). Oil's optical properties are tricky as they change across the electromagnetic spectrum. In the ultra-violet, visible, and near-infrared portions, water is more reflective than crude oil (Andreou & Karathanassi 2011, Fingas & Brown 2014); however, moving into the longer wavelengths such as TIR, the reflectance of the oil becomes slightly greater (Goodman 1994). The Sun emits the bulk of its energy in the ultraviolet and visible light range so hypothetically more absorption of solar radiation into the oil will occur as more light hits the oil. This coupled with the lower heat capacity of oil compared to water means that it might be possible for oil spills to appear warmer than water during the daytime and cool faster at night. However, little work has been done on comparing broad-scale, long-term oil spill temperatures to SSTs. Interestingly, when viewing SSTs, the thickness of the oil slick plays a major role. Oil slicks between 50 and 250 μm exhibit temperatures very close to the surrounding ocean due to heating from the ocean with evaporation canceling out incoming solar radiation over time while thicker (250 – 500 μm) oil patches are warmer than the surrounding ocean during the day (Ying et al. 2009). SSTs could be used most effectively to identify the oil spill extent, however, when the oil has yet to be dispersed while thickness is still great (Inmann et al. 2010).

The results could break down the standard land/sea breeze cycle. During the daytime hours, a sea breeze is formed from the land surface warming faster than the ocean, followed by the creation of low and high pressures, respectively. The resulting breeze flows from the sea to

the land. However, when oil is present the additional warming could reduce the gradient between the sea and land. In addition, the increased temperatures over the oil slick would produce more convection and subsequently more precipitation. Figure 2.1 shows the hypothesized influence of a large oil spill on nearby meteorological conditions. Figure 2.2 shows an example of a day when anomalous showers developed over the slick.

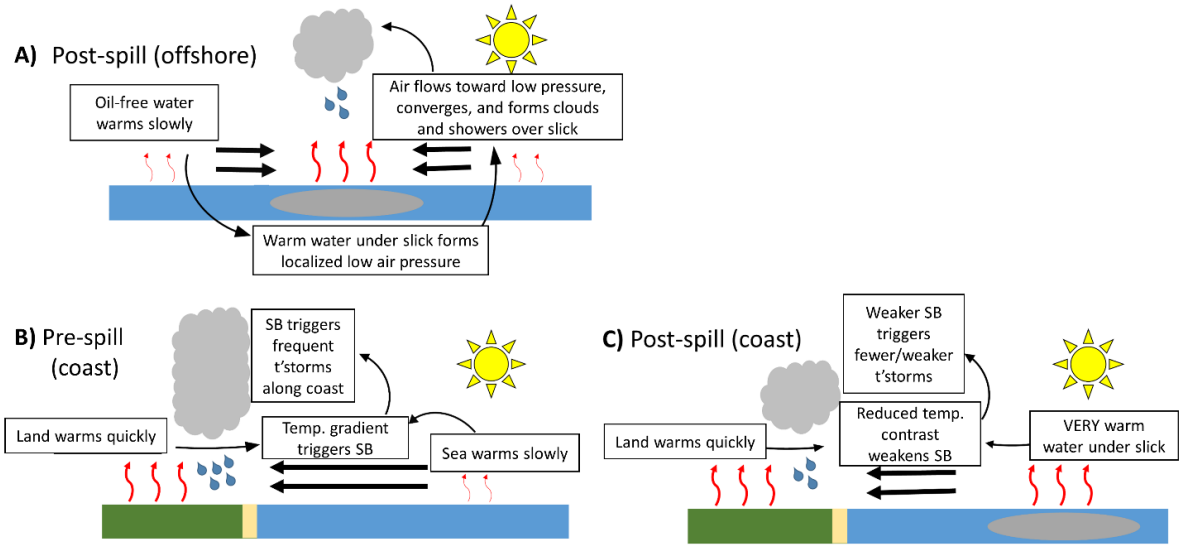

Figure 2.1. Oil influence on sea breezes. (A) Hypothesized post-spill effects on clouds and precipitation over the slick. (B) Normal (i.e., pre-spill) sea breeze (SB) conditions near the coast compared to (C) Post-spill, oil-modified SB circulation. Taken from Miller (2022a).

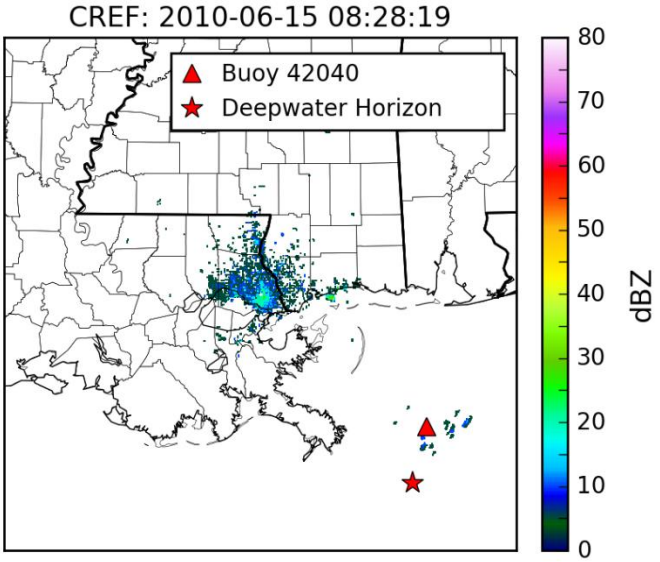

Figure 2.2. Radar reflectivity on 15 June 2010. Taken from Miller (2022b).

When oil is released into the ocean, a wide range of processes alter or break down the oil. The most common are evaporation, emulsification, photo-oxidation, and biodegradation, with each having its own impact on the ability of chemical oil dispersants (Nordvik 1999). Since the 2010 oil spill, research into photo-oxidation has grown tremendously as it was determined that this weathering process has a much higher impact than previously thought (Aeppli 2022). Through indirect photo-oxidation, new oxygen species are created within the oil that oxidizes surrounding oil compounds and inhibit dispersants' ability to function by 30 – 50% (Ward et al. 2020, Aeppli et al. 2022). Since most of the weathering process for photo-oxidation takes place within the first week (Ward et al. 2020) this chemical alteration of the oil would contribute to a longer-lasting oil slick.

2.5. Urban Heat Island Effect

Because the meteorological effects of oil spills have yet to receive scientific study, context for the atmospheric circulatory impacts must be drawn from analogous Earth-system

occurrences. Phenomena such as the urban heat island (UHI) effect, which results from the difference in temperature between an urban environment and the surrounding rural one, could provide an analogue to the heating of the atmosphere over an oil slick. Originally coined by Manley (1958) on snowfall accumulation in urban England, the UHI effect involves is the comparison of a warm city in a metaphorical "sea" of otherwise cooler locales. Although Manley believed the effect to be small, in subsequent years it was realized this effect was far larger than anticipated and presently is an active research topic (Deilami et al. 2018).

The UHI effect is generated through an increase in the air temperature above a city due to several factors. The physical properties of building materials abundant in these settings store heat and release it slowly over time to the surrounding urban landscape. In addition, urbanization minimizes latent heat flux provided by vegetation, but it increases the sensible heat flux resulting from the absorption of incoming shortwave solar radiation by highly absorptive materials common to metropolitan areas (Price 1979, Imhoff et al. 2010). Magnitudes of the temperature range from the UHI effect vary greatly. Depending on vegetation and seasonality there could be a temperature difference upwards of two Celsius degrees (Price 1979, Armson et al. 2012). The diurnal cycle is another factor of the UHI effect. In the early morning, the temperature difference between a city and the countryside would be significantly smaller than the difference during the afternoon or evening. The UHI reaches its peak influence a few hours after sunset (Zhou et al. 2013). During the nighttime, however, there is no incoming solar radiation for a city to absorb so the temperature differences decrease (Dewan et al. 2021, Stone & Rodgers 2001, Zhou et al., 2013). Regionality and seasonality are other ways the UHI is altered (e.g., a forest versus an arid shrub-land). Winter produces a different UHI effect than summer. Due to the moisture in vegetation, areas of grassland or forest have a great temperature

difference from neighboring urban environments while arid regions exhibit a smaller difference, but a desert will have miniscule temperature difference between a city and the surrounding environment (Imhoff et al. 2010). Similarly, the UHI effect is greatest during the summer when more vegetation exists outside of a city. In the winter, the temperature difference between urban and vegetated landscape decreases from the lack of solar radiation and vegetation to evapotranspirate (Chun & Guldmann 2018, Deilami et al. 2018).

The comparison between the heated GOM at the oil slick and the UHI continues when considering precipitation impacts. The urban rainfall effect (URE) is the direct result of the UHI and describes how a metropolitan landscape bolsters the intensity, but not the frequency, of late-afternoon, convective-based rainstorms (Changnon et al. 1976, Shepherd et al. 2010). As the urban-induced heating causes increased convection, the rough urban topography also contributes to the increased precipitation (Hjelmfelt 1982, Bornstein & Lin 2000, Shepherd et al. 2010). Although the ocean lacks the ability to perturb the boundary layer in the same way that buildings can, additional heating provided by the oil's presence could still cause an impact on precipitation intensity.

The same concept applies to lightning as well, as lightning generation from thunderstorms is largely a result of convective processes (Williams 1994, Pinto et al. 2013). An increase in convection intensity would presumably lead to an increase in lightning strikes as well, but the increase in lightning also comes from aerosols produced over cities (Stallins & Rose 2008). While aerosol concentrations would likely be smaller over an oil slick, the evaporation of oil on the ocean surface as well as the controlled burnings of oil could cause a sufficient addition of aerosols to create anomalous strikes (Perring et al. 2011, Rudich et al. 2003, Gullet et al. 2016, Gullet et al. 2017).

The UHI could be an analogue to the oil spill as the oil would increase the amount of solar radiation absorption at the sea surface relative to the surrounding water. The overlying air mass would take on the characteristics of the newly altered surface temperature increasing the temperature and instability of the air above the oil slick. However, an understanding of the environment and spill timing is necessary to determine how the oil slick may have elevated SSTs.

Chapter 3. Research Design

3.1. Synoptic Context and SST Overview

The summer of 2010 (May-August) was unusually warm for the southeastern United States. At the time, it had become the fourth-warmest summer for the U.S., and several states within the Southeast broke temperature records over the summer months (NOAA 2011). These warm conditions were also manifested in the Gulf of Mexico, where SSTs are illustrated within the 0.25-degree ERA5 Reanalysis (Figure 3.1, Hersbach et al. 2020). The warmest portions follow the general outline of the Gulf shelf and coastlines. These temperature abnormalities were largely attributed to the Azores High (also known as the Bermuda High and/or North Atlantic Subtropical High, NOAA 2011). This encroaching, semi-permanent anti-cyclone is a common occurrence for the southeastern United States. The anomalous strength of this circulation brought hot, humid, and sunny conditions across the Southeast. The duration and intensity of the Azores High were both above average (Figure 3.2) according to the Bermuda High Index (Stahle & Cleaveland 1996, Debbage et al. 2017), allowing for a much warmer summer and inhibiting major tropical storms from forming within the Gulf. Figure 3.2 shows that the Azores High was strongest in May and June and both months showed reasonable SST differences of about one to two Celsius degrees above the climatological average (Figure 3.1B-C). June showed a stronger SST difference than May, possibly due to being farther along in the summer resulting in an additional amount of solar energy absorption. The above-average temperatures continued through July and August with July having the smallest warm anomaly. The diminished warm anomaly in July was caused most likely by the double impact of Hurricane Alex making landfall on 30 June and Tropical Depression Two making landfall on 8 July, with both landing in northeastern Mexico (Gutro 2010, NWS no date).

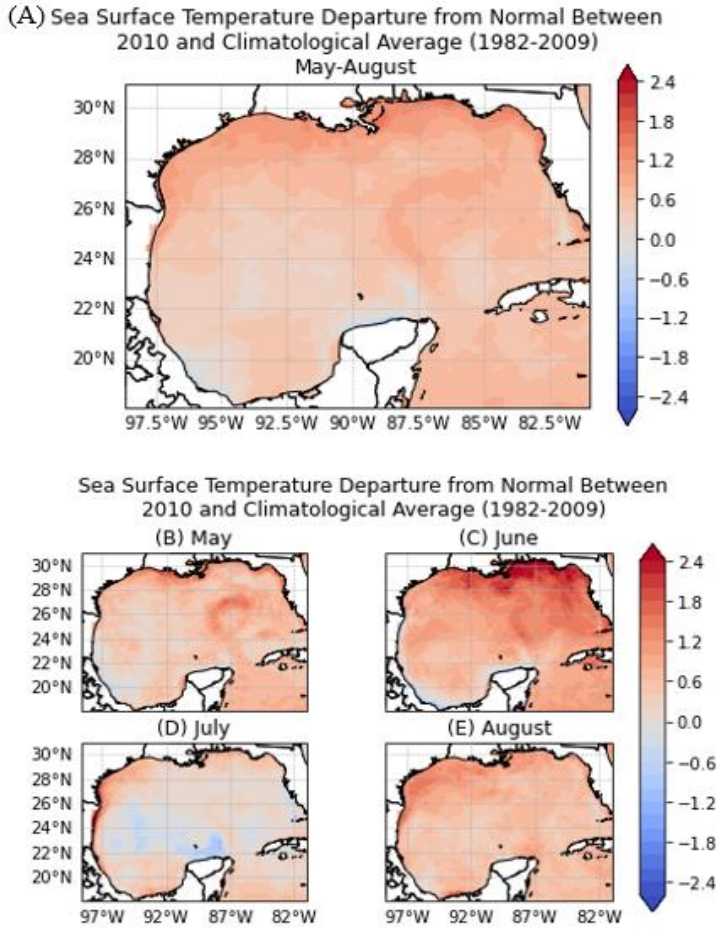

Figure 3.1. (A) Averaged SSTs created from ERA5 Reanalysis data from May-August of 2010 compared to the 30-year climatological average (1980 – 2009). (B)-(E) Averaged SSTs from May-August of 2010 compared to the 30-year climatological average (1980 – 2009) per month.

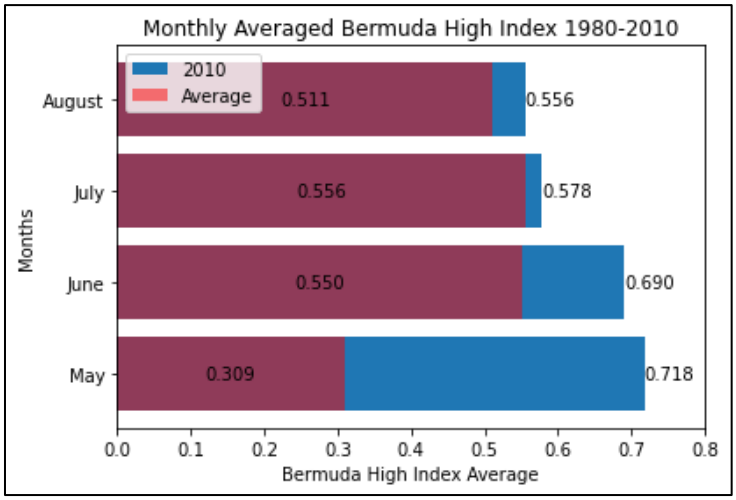

Figure 3.2. Averaged Bermuda High Index 2010 compared to the 30-year climatological average (1980 – 2009).

3.2. *In-situ* Data and Oil-Overlapping Buoys

The publicly accessible NOAA Environmental Response Management Application (ERMA) was used to determine the location and extent of the oil (https://erma.noaa.gov/gulfofmexico/erma.html). Daily footprints were generated using a Texture Classifying Neural Network Algorithm (TCNNA; Jacobi et al. 2008) applied to SAR satellite data and released in shapefile format. The shapefiles were then converted into raster data within ArcGIS with 50 m cell sizes (ERMA Gulf of Mexico 2022). The data covers 23 April 2010 to 11 August 0210. However, of these 111 days, only 88 have data completeness, and some days lack a comprehensive view of the oil. Despite these limitations, the TCNNA SAR footprints still provide a useful ability to identify the general location and near-daily spread of the oil spill.

Figure 3.3 shows a frequency map highlighting the regions with the greatest oil concentration from the 88 days given by the TCNNA footprints and NOAA ocean buoys collected from the NOAA National Data Buoy Center. Buoy 42040 is the closest to the center of the oil spill, and this location is also where some of the highest temperatures should be seen. In fact, Buoy 42040 was within the oil slick on 46 of the 88 available days (52%) with oil footprints (Table 3.1).

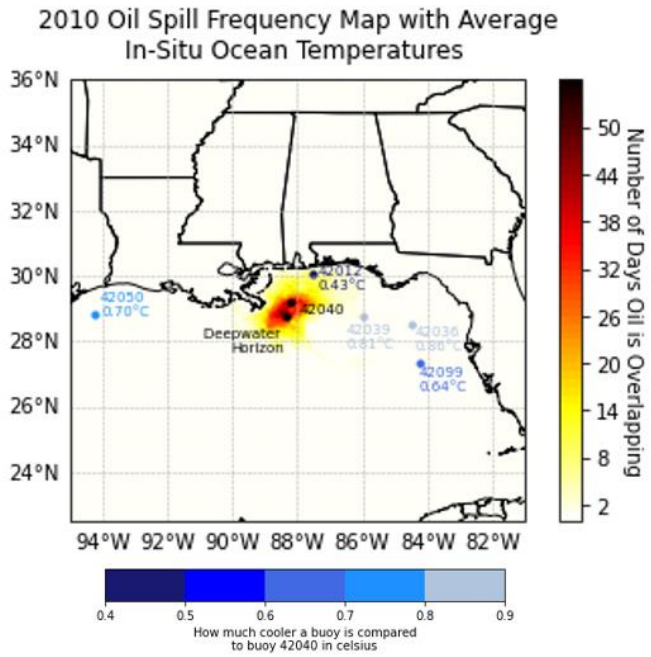

Figure 3.3. 2010 oil spill frequency map with buoy stations color-coded by temperature departure from Buoy 42040.

Table 3.1. NOAA Buoy Metadata

Buoy ID	Depth ocean temperature is recorded (m)	Approximate distance from the coast (km)	Approximate distance from *Deepwater Horizon* (km)	Percent of days covered by oil	Temperature Departure from Buoy 42040 (°C)
42012	2	23	167	9%	–0.43
42036	1.5	145	377	0%	–0.86
42039	1.5	120	230	1%	–0.81
42040	1.5	90	53	45%	–
42050	2	76	573	0%	–0.70
42099	0.46	151	430	0%	–0.64

3.3. Comparison of Satellite SSTs and *in-situ* data

Stations 42036, 42039, and 42040 had continuous historic climatological data dating back to 1994, 1996, and 1996 respectively. All three of these show the same basic pattern with 2010 ocean temperatures warming beyond the historical average in mid-May, followed by above-average mid-June temperatures to about 30°C or in the case of 42040 beyond 32°C (Figure 3.4). In early July 2010, the SSTs drop below the historical average. Along the coast, the

trend shows much the same pattern, with temperatures being above average farther inland but closer to average near the shoreline (NOAA 2011). However, starting at the end of July, another large spike in ocean temperatures appears across all three stations. Stations 42039 and 42040 follow each other quite well and exhibit the same trends, with 42039 having a smaller difference between 2010 and the historic data. Station 42036 is the farthest away from the oil spill and features many days in 2010 when the temperature drops by a degree or more and then quickly rebounds. It follows the same basic pattern, but in a much more disorganized manner. This station also has the lowest temperature of the three stations with peaks in mid-June and late July barely exceeding 30°C. All three buoys contain sporadic missing hourly data.

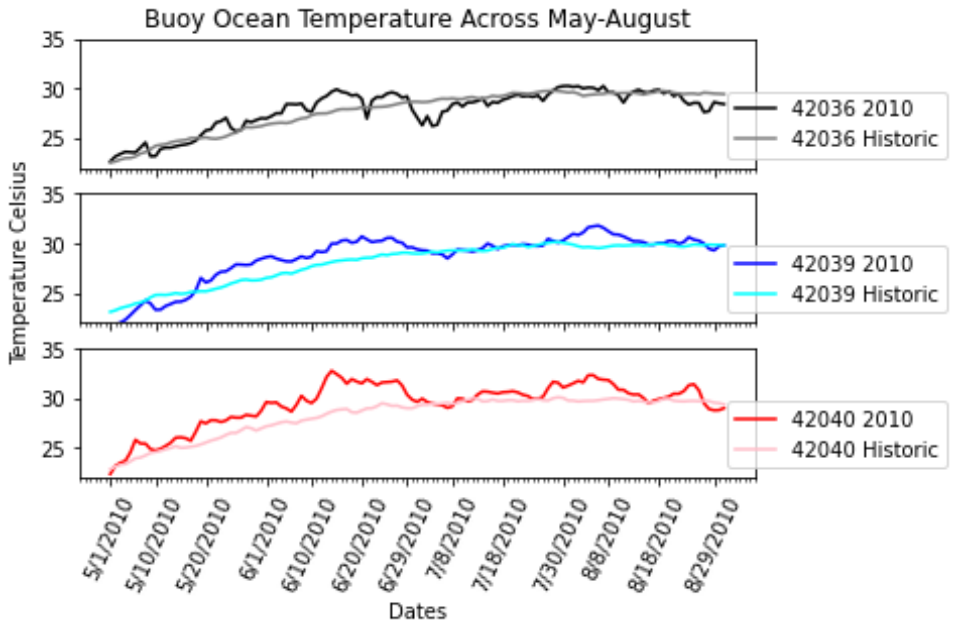

Figure 3.4. Sea surface temperatures measured across May-August for Buoys 42036, 42039, and 42040, compared to historic values dating back to the initial recording of ocean temperatures (1994, 1996, 1996 respectively; Data retrieved from the National Data Buoy Center 1971).

To assess the atmospheric impacts of the oil spill, an understanding of the slick's thermodynamic qualities is needed. Because numerous SST data sets are available, this section compares remotely sensed SST reanalysis with observed *in-situ* data to establish consistency.

Six buoy stations with periods of record extending to 2010 and containing ocean temperature were examined. Each station was compared to the Advanced Very High Resolution Radiometer (AVHRR) reanalysis (Merchant et al. 2019, Copernicus-ECMWF 2022, NOAA CoastWatch 2022) SST values for the nearest cell within 1.5 km of the buoy. The Level-4 Multi-Product Combined AVHRR dataset was chosen for this comparison as it offers a 0.05-degree resolution whereas the ERA5 SST reanalysis offers a 0.25-degree resolution, allowing a more accurate representation of the buoy locations. However, this still is a wide area measured compared to the buoy. The depth of the *in-situ* ocean temperature measurement varied per station (Table 3.1), with most *in-situ* water temperatures collected at least 1.5 m below the surface. See Figure 3.3 for the locations and IDs of all six buoys.

When examining each buoy across the summer, stations 42012 and 42050 showed a lower *in-situ* temperature than AVHRR reanalysis (Table 3.2), with the other four stations showing the opposite (i.e., warmer *in-situ* than remotely sensed estimates). Buoys 42012, 42040, and 42050 are the closest to the shore as well. Station 42050 was the only site displaying a higher AVHRR temperature in both median and mean, but this station was the farthest away from the epicenter of the oil spill. Although Station 42012 was much closer to shore than any other, it showed a very small difference in mean temperature between *in-situ* and AVHRR. This station was also the second closest to the *Deepwater Horizon* at roughly 150 km from the center. It is possible that proximity to the coastline and depth of water influenced the mean and median temperatures for both the *in-situ* and AVHRR.

Table 3.2. Mean and median ocean temperatures of *in-situ* and SSTs of AVHRR Reanalysis in degrees Celsius.

	Buoy Ocean Temperatures		AVHRR Reanalysis SSTs		Difference between in-situ and AVHRR Reanalysis SSTs	
Buoy Station	Mean	Median	Mean	Median	Mean	Median
42012	29.02	29.75	29.05	29.65	-0.03	0.10
42036	28.59	29.47	28.43	29.39	0.16	0.08
42039	28.64	29.57	28.46	29.36	0.18	0.21
42040	29.45	29.94	29.16	29.80	0.29	0.14
42050	28.75	29.79	28.80	30.12	-0.05	-0.33
42099	28.81	29.47	28.70	29.29	0.11	0.18

When comparing each buoy to site 42040, the closest to the center of the oil spill, the average temperature across the summer was higher at buoy 42040 by a range from +0.43 C° to +0.86 C°. This trend is mirrored within the AVHRR data as well, although not quite to the degree of the *in-situ* data. In both the *in-situ* and AVHRR data, Station 42012 had the smallest difference from Station 42040. Thus, *in-situ* data suggests waters near the slick were at least approximately 0.5 – 1 C° warmer than the surrounding Gulf waters.

3.4. Model Initialization

To simulate the oil spill, the Weather Research and Forecasting (WRF) model version 4.2 (Skamarock et al. 2019) is used by increasing SSTs at the site of the oil slick. WRF is a common tool used to identify atmospheric alterations from land-cover changes (e.g., Miller et al. 2019, Román-Cascón et al. 2021), and input files within a WRF simulation can be used to manipulate the landscape based on the boundary condition provided by the static geography input files. Additionally, nesting domains within WRF allows for much higher spatial resolutions than the ERA5 Reanalysis boundary conditions provide. These factors allow for the study of events at a finer scale than would otherwise be feasible. The WRF numerical modeling is conducted to

discover the extent to which the oil spill influenced meteorological conditions during summer 2010.

While WRF cannot assimilate the presence of oil in the ocean directly, it can emulate the potential symptoms of an oil spill. Because the SSTs would increase as the darker sheen on the surface would absorb more solar radiation (Figure 2.1), the elevated SST signature can be mimicked within the model. Four different methods of assimilating slick-enhanced SSTs were employed, and although the oil moved from day to day, this is not feasible to simulate within each experimental scenario. To compensate for this, the experimental simulations are all guided by the spatial distribution of TCNNA oiling footprints shown in Figure 3.3. By using this frequency map, the areas of greatest impact can be determined by the areas of greatest frequency. The primary scenario of interest is termed Buoy 42040 Constant (B40C). This "constant" scenario features a ubiquitously increased SST across the entire oil slick footprint regardless of frequency. The elevation amount for B40C was 0.688 C° at each point within the oil slick footprint. The secondary scenarios are the "decay" simulations and are primarily used to determine the sensitivity of the WRF models to perturbations in the elevated SST signatures. These three have SST elevations at a maximum where the frequency was at the highest in Figure 3.3 (56 out of the 88 total days or a maximum frequency of 64%). The first of the decay scenarios is Buoy 42040 Decay (B40D), in which SSTs were increased by 0.437 C° on the oil slick footprint where the frequency was at 64% and at each lower frequency increment (i.e., 1/88 = 1.136%), the SST elevation on the oil slick footprint was decreased by 0.0078 C° until the frequency equaled 0%. The second decay scenario is Buoy 42040 Elevated Decay (B40ED). This scenario is identical to B40D except that the highest frequency portion of the footprint is elevated by 1.909 C° then decreased by 0.0341 C° at each lower frequency increment. The final

experimental scenario is AVHRR 42040 Decay (A40D) as this model was based on the remotely sensed AVHRR temperatures. Again, this model is identical to B40D except it is elevated at the highest oiling frequency (i.e., 64%) by 0.300 C° with a decrease of 0.0340 C° at each lower frequency increment.

The observed ocean temperatures collected by NOAA buoys across the GOM (Table 3.2) guided how strongly SSTs should be raised in the oil footprint. Buoy 42040, the closest and most frequently oil-encountering buoy to *Deepwater Horizon* (Figure 3.3), showed an average temperature of 0.688°C higher than the other buoys. Table 3.3 shows the degree to which each scenario's oil slick was elevated as well as how SSTs were decreased for each lower frequency increment of Figure 3.3. However, because Figure 3.4 demonstrated that near the slick, water temperature differences gradually increased from the long-term average, maximum SST increases were also introduced to the WRF scenarios gradually (Figure 3.5). The maximum SST increases indicated in Table 3.3 were achieved using a linear interpolation beginning on 0000 UTC April 22 and peaking on 1800 UTC June 14. Between these two dates, the WRF ocean input files contained 215 SST fields separated by six hours. As the simulation successively reached each new six-hourly ocean input field, the SSTs were increased by an additional 0.465% of the maximum warming for that scenario, and by 1800 UTC 14 June 2010, each scenario would experience its maximum SST anomaly (215 x 0.00465 = 1.0). June 14 was chosen as the apex because it displays the peak SST abnormality in Figure 3.4. After reaching this apex, the same linear interpolation was repeated in reverse for the 232 six-hourly timesteps between 0000 UTC June 15 to 1800 UTC August 11 until the ratio would equal zero. Each of these experimental scenarios will be compared to a control model where no oil slick is incorporated.

Table 3.3. Scenario names and abbreviations and model SST elevation dispersion.

Scenario Name	Abbreviation	Highest elevated SST	Decrease in elevated SST per decrease in frequency of oil overlap
Buoy 42040 Constant	B40C	0.688°C	–
Buoy 42040 Decay	B40D	0.437°C	0.0078181°C
Buoy 42040 Elevated Decay	B40ED	1.909°C	0.03409091°C
AVHRR 42040 Decay	A40D	0.30016°C	0.00536°C

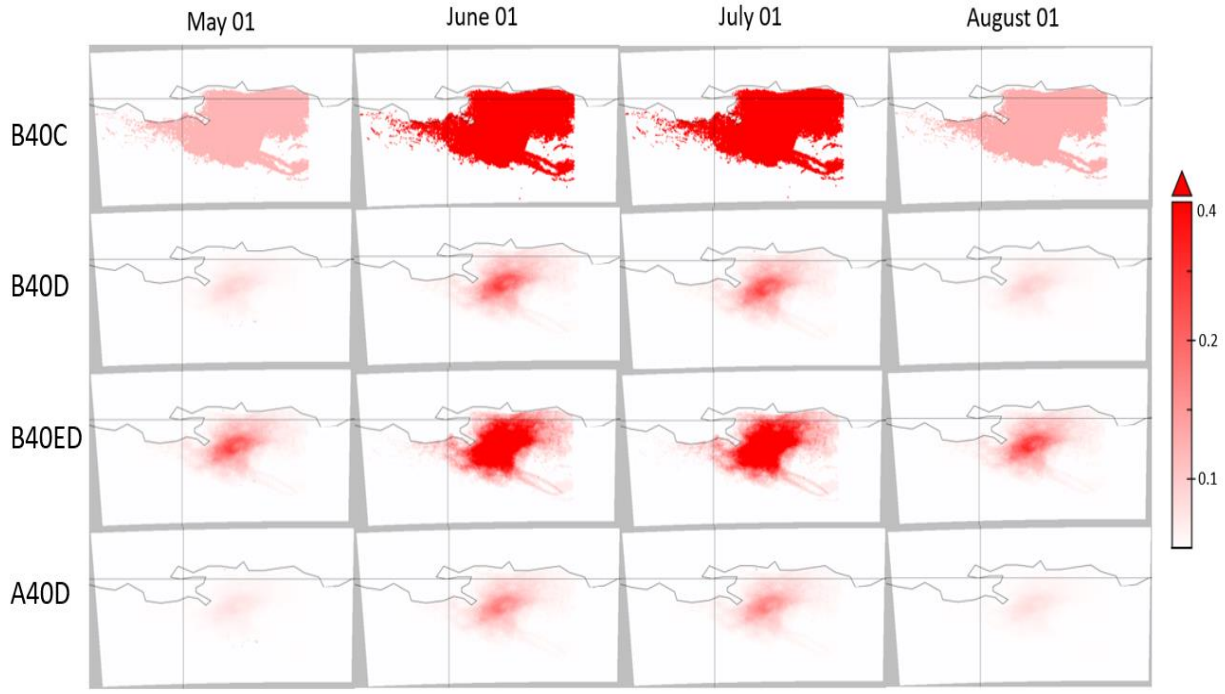

Figure 3.5. WRF SST elevation frequency and location. Each scenario reaches its peak SST increase on 14 June 2010.

Each model is run from 10 April 2010 0000 UTC to 31 August 2010 1800 UTC with output every six hours and 10 – 20 April discarded as the model's spin-up time. The ECMWF ERA5 Reanalysis on single and pressure levels was used as the boundary conditions (Hersbach et al. 2020) and applied at six-hourly timesteps for the length of the model run. Two domains were used with the parent domain encompassing the southeastern U. S. and the inner, two-way nested domain capturing the northern GOM and lower portion of Louisiana, Mississippi, Alabama, and Florida (Figure 3.6). Table 3.4 shows the parameterizations used within the

models, which were guided by previous studies WRF modeling studies in similar regional contexts (Miller et al. 2019, Dyer & Rigby 2020, Srivastava et al. 2023) as well as pilot testing.

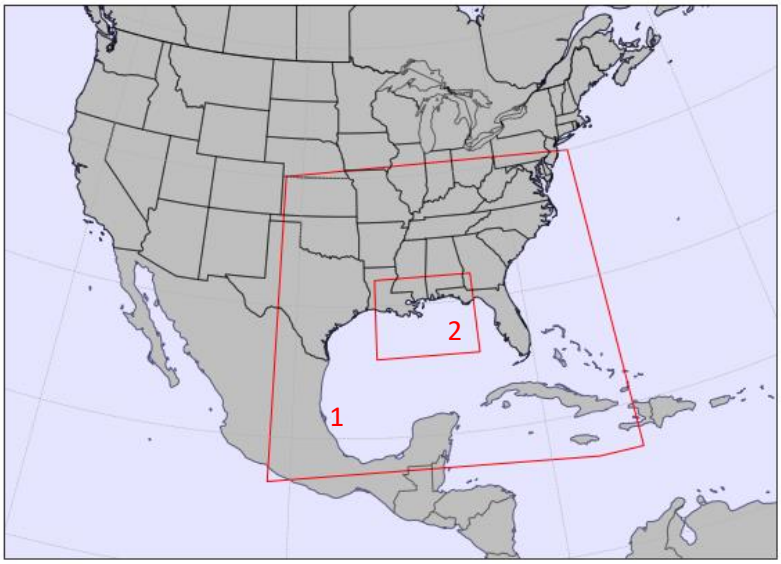

Figure 3.6. WRF domains.

Table 3.4. WRF parameterization schemes.

Setting	Scheme
Cumulus	New Tiedtke
Microphysics	WRF Double-Moment 6-Class
Boundary Layer	Mellor-Yamada-Janjic
Radiation	RRTMG
Boundary Conditions	ERA5 Reanalysis
Vertical Layers	40
Horizontal Grid Spacing	12 km, 4 km
Land-Surface	Unified Noah land-surface

3.5. Data Analysis Methods

3.5.1. Model verification

The WRF control simulation is validated against surface observations of sea level pressure (SLP), 2-m air temperature, and 10-m wind speed. Four buoys within the inner domain supplied the observations (Figure 3.6), which were retrieved from the National Oceanic and Atmospheric Administration's National Data Buoy Center (NOAA NDBC). Model accumulated precipitation was validated qualitatively through the Integrated Multi-Satellite Retrievals for Global Precipitation Measurement (IMERG) final run for the daily accumulated precipitation with gauge calibration and combined microwave-IR estimate (GPM_3IMERGM v06) (Huffman et al. 2015). The model performance is characterized using the coefficient of determination (R^2) to determine the correlation between each model and the observations (See Section 4.1).

3.5.2. Experimental analysis

For both the control and experimental models, monthly averages were generated from the 6-hourly WRF output files. These were then differenced to examine the effects of the experimental conditions on the resolved meteorological patterns. The variables examined include 2-m temperature, 2-m dewpoint, SLP, 10-m wind speeds and direction, cloud fraction, and accumulated precipitation. These results were compared spatially and temporally using significance tests with a 95% confidence interval for their differences at each cell. While 2-m temperature and precipitation are provided directly in the WRF output, the python scripting package WRF-Python was used to calculate SLP, 2-m dewpoint, 10-m windspeeds, and cloud fraction at low, mid, and high levels. Comparisons were conducted for the entire inner domain (Figure 3.6); output for the coarser parent domain was not examined. Statistical significance was calculated in Python by computing the difference between the experimental model minus the

control at each temporal increment (i.e., six-hourly, daily, etc.). The 95% confidence interval associated with the mean difference was determined, and differences, both positive and negative, were deemed statistically significant if the 95% confidence interval did not contain zero.

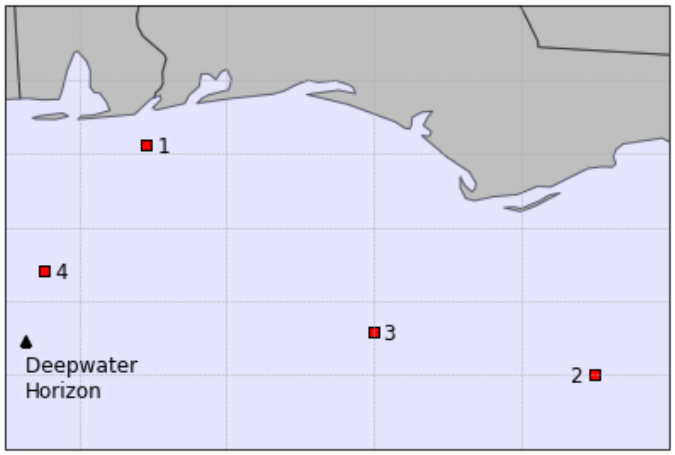

Figure 3.7. Buoy validation sites where: (1) Buoy 42012, (2) Buoy 42036, (3) Buoy 42039, (4) Buoy 4240.

3.6. Limitations

While WRF is a powerful tool capable of simulating hypothetical scenarios, this study cannot incorporate all the elements necessary to make these simulations completely accurate. As previously stated, WRF has no actual capacity for incorporating oil so the method of elevating SSTs is a brute force tactic designed to assess the sensitivity of coastal weather conditions to oil-elevated SSTs versus a model without oil. While it mimics the thermal signature of the SST footprint, it does not actually modify the physical properties of the water in a way consistent with the oiling (i.e., albedo, air-sea exchange). The oil slick moved from day to day, so the static frequency map only approximates the average effect of the oil slick. Additionally, the warm summertime Mississippi River discharge into the GOM likely played a role in elevating and stratifying coastal SSTs.

Chapter 4. Results

4.1. Model Validation

The B40C scenario was compared against the observed data as the experimental run, in theory, should be closer to the observed conditions than the control run. R^2 values for 2-m air temperature and SLP (Table 4.1 – 4.2) were used to validate the model's accuracy at six-hour intervals with observed data from the four buoys within the inner domain of the WRF model. The cell nearest to the buoys' coordinates was used which means that no model-generated variables exceeded 1.5 km separation from the corresponding buoy. Table 4.1 shows a strong positive correlation with the observed 2-m air temperatures. B40C had R^2 values between 0.79 and 0.87 with most buoy locations being in the 0.80s. Stations 42012 and 42040 showed the weakest R^2 values with 42040 being the lowest at 0.79. Buoy 42036 had the highest R^2 value and was the farthest from the oil footprint with Buoy 42039 the second farthest.

Table 4.1. Correlation of 2-m air temperature and buoy-measured air temperature using R^2 values.

Buoy ID	Buoy Thermometer Height (m)	B40C
42012	3.4	0.82
42036	3.7	0.87
42039	3.7	0.85
42040	3.7	0.79

SLP correlation is almost ubiquitously higher than the 2-m air temperature values (Table 4.2). Buoys across the model largely feature SLP R^2 values in the mid-to-high 0.80s. Where the

2-m air temperature showed stronger correlations with buoys 42036 and 42039, SLP shows higher correlations with buoys 42012 and 42040.

Table 4.2. Correlation of SLP and buoy-measured pressure using R^2 values.

Buoy ID	Buoy Barometer Height (m)	B40C
42012	2.4	0.87
42036	2.7	0.85
42039	2.7	0.86
42040	2.7	0.88

In addition to SLP and 2-m air temperature, R^2 values for wind speed were also computed between the observed data and B40C (not shown). While the R^2 values were relatively small, between the 0.10s and 0.20s, the WRF simulation accurately captured the most important aspect of the diurnal cycle compared to the observed data (Figure 4.1). Figure 4.1 shows how the mean wind speed compares to the observed wind speed. The B40C resolved slower-than-observed wind speed at all four locations, but for buoys 42036 and 42039 the diurnal wind speed patterns stay consistent with the observed. For buoy 42040, the B40C diurnal wind speed pattern deviates from the observed between 1200 and 1800 UTC when the modeled winds slow whereas the observed winds accelerate. The modeled winds at buoy 42012 largely did not successfully match up with the observed wind data. This could be a result of the buoy being close enough to the coastline that the model had a difficult time transitioning between the two surface fields; however, the mean windspeeds for 0000 and 1800 UTC were nearly congruent with the observed which outperformed all other buoys.

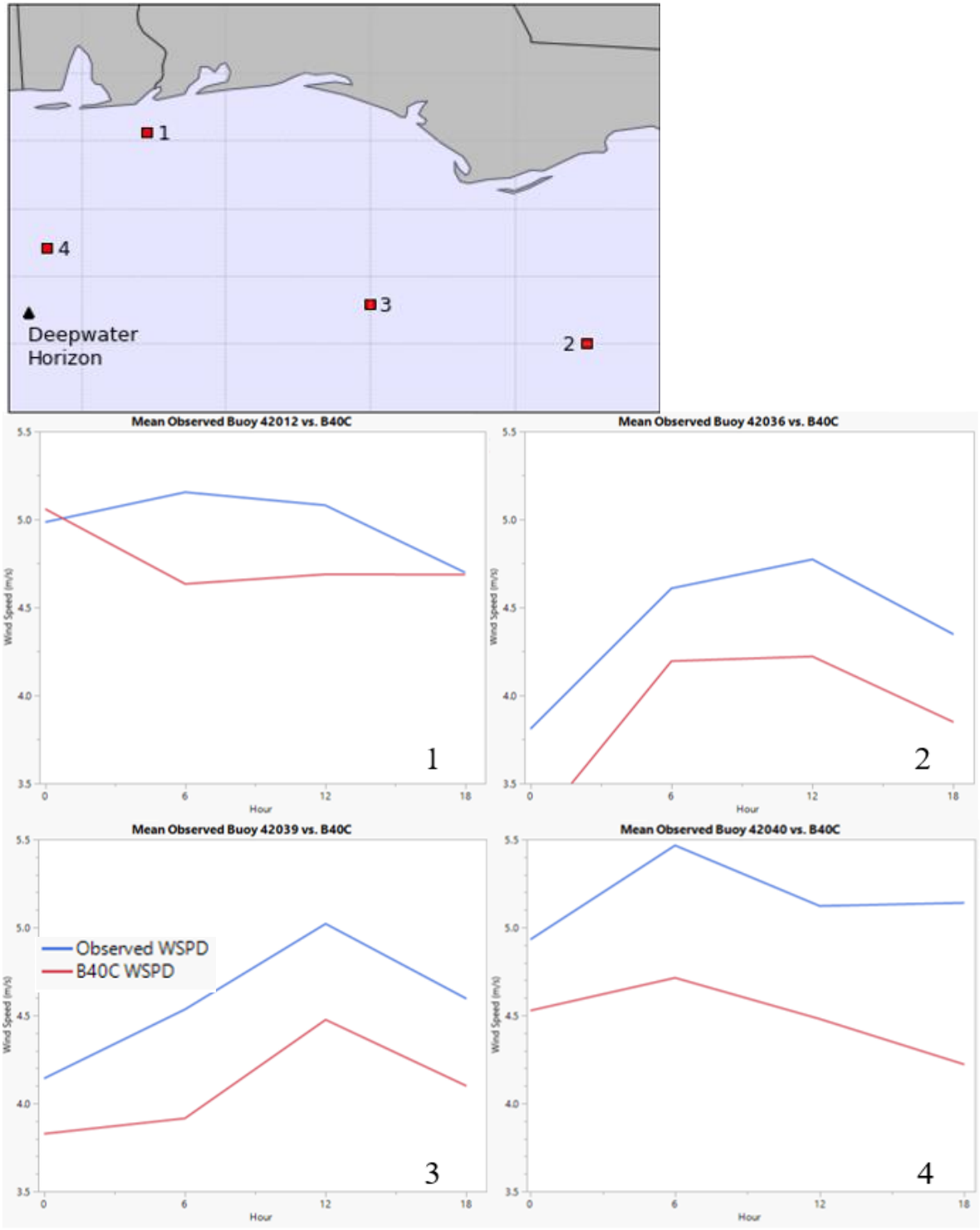

Figure 4.1. Mean buoy-measured observed wind speed versus mean modeled wind speed at six-hour intervals.

4.2. Changes in 2-m Air Temperature and 2-m Dew Point

Due to the importance of summertime convection in cloud and precipitation development in the GOM, the 2-m air temperature (T2) changes are hypothesized to be the basis for potential meteorological changes. For B40C, immediately in May the SST influence is apparent in the T2s and follows the same trend as the SST enhancement written into WRF by maximizing in June (Figure 4.2). July exhibits a swath of T2 lower B40C difference values, roughly –0.1°C to –0.2°C, south of the oil footprint which lasts into August indicated by the black arrow labeled 1 in Figure 4.2C and Figure 4.2D. Starting in May and then growing across the months until August, there are values of –0.4°C or lower along the interior coastline, although, along the Mississippi-Alabama border, there is a small, diagonally oriented region of roughly equivalent T2s across all months.

The changes in 2-m dew point temperatures (TD2) are shown in Figure 4.3. B40C displays higher TD2s across the oil footprint's rough region, albeit more scattered and less coherent. Mirroring what was seen in the July T2s, there is a continuous zone of higher control model TD2s in the southwestern region of the domain and higher B40C TD2s concentrated in the northern tier of the domain (Figure 4.3C). August too has a small area of higher control model TD2s that matches up with the T2s on the eastern central section of the domain. Interestingly, while the control model has higher T2s over the Louisiana-Mississippi region for July, the control has significantly lower TD2s in the same area indicating B40C has a smaller dewpoint depression.

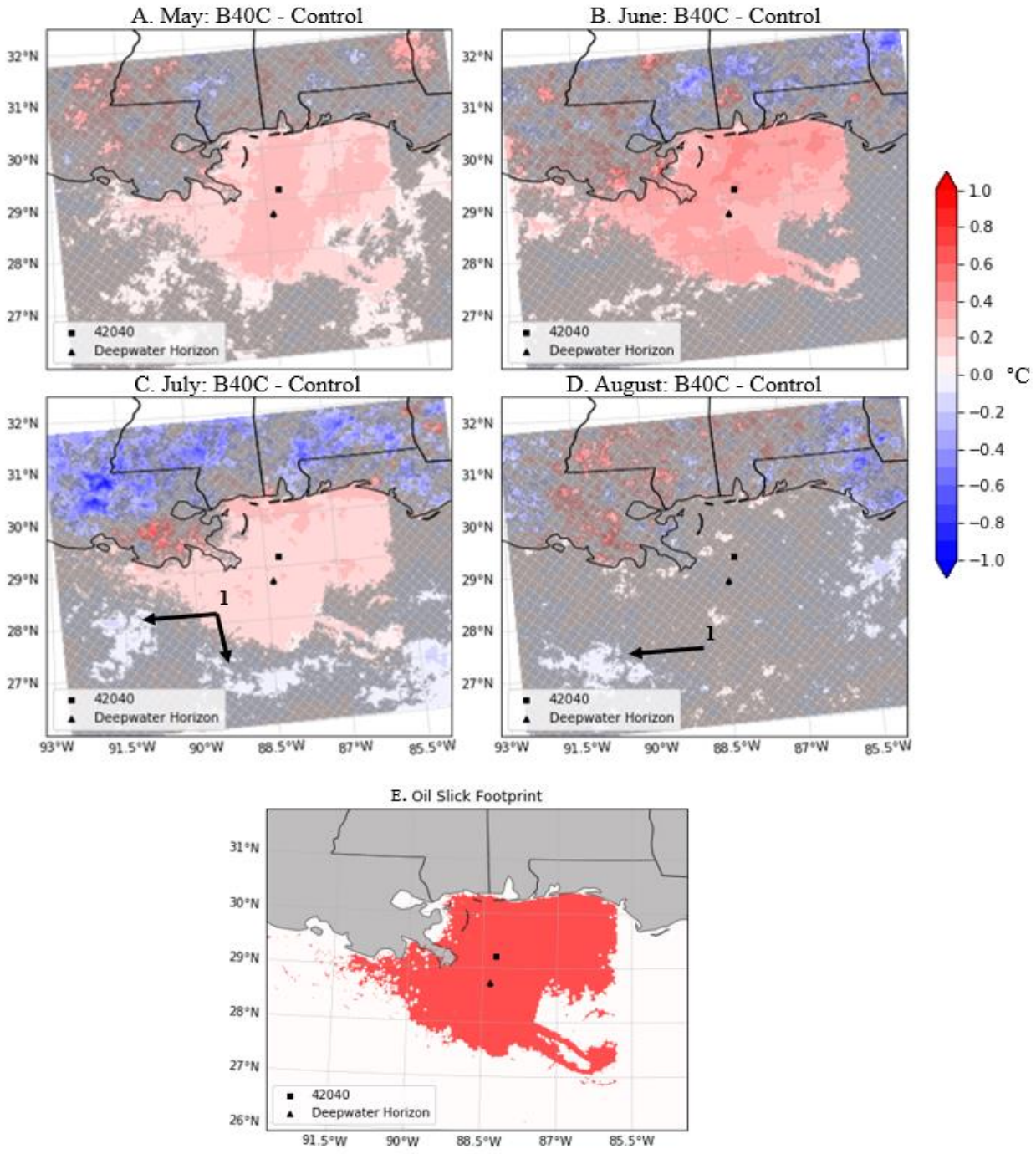

Figure 4.2. Differences in mean T2 between experimental scenario B40C minus the control for A) May, B) June, C) July, and D) August, where the cooler values are indicated by blue and warmer values with red. Stippled areas indicate statistical insignificance with a 95% confidence. E) Oil slick footprint is shown for reference.

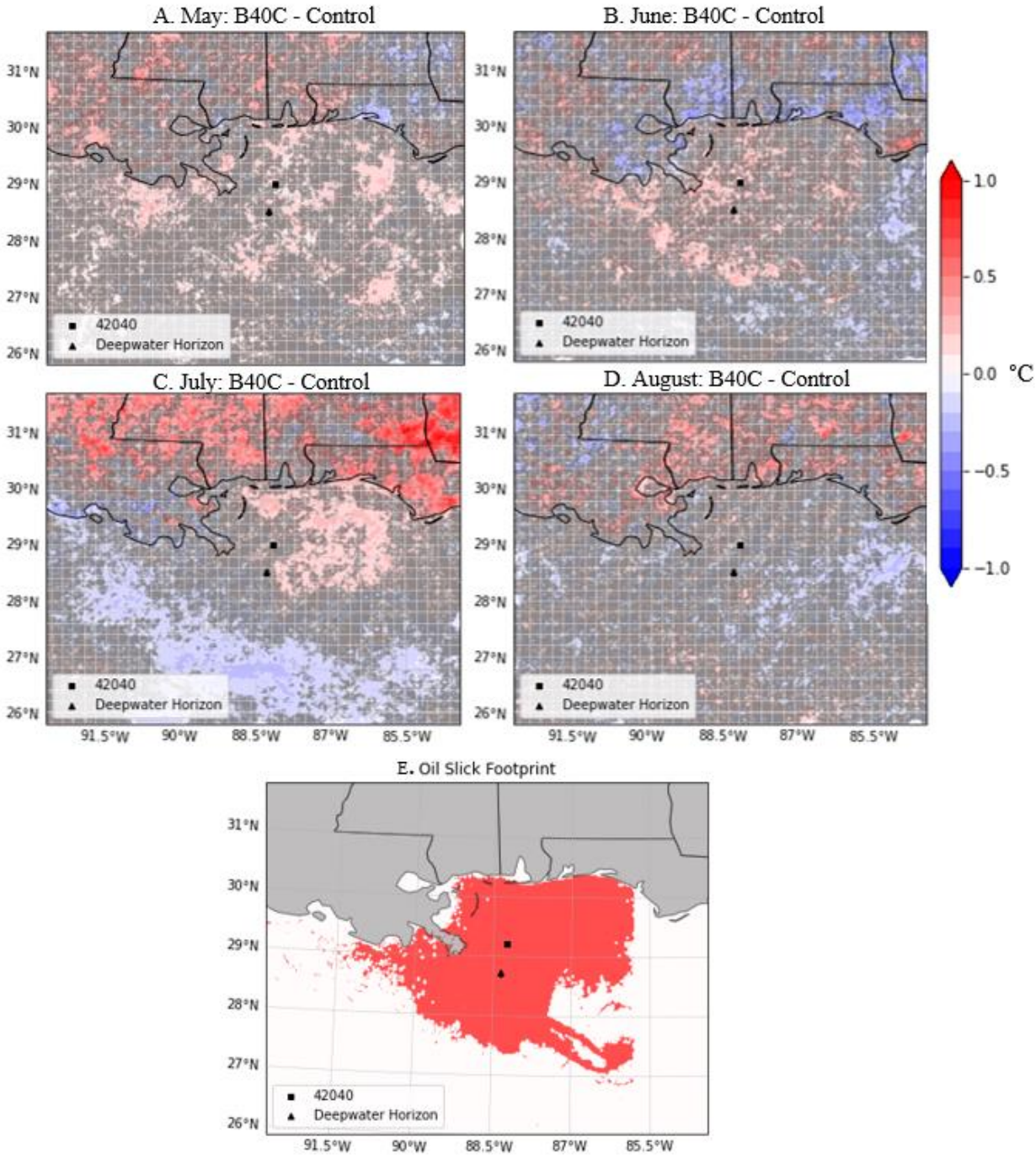

Figure 4.3. Same as Figure 4.2 except for 2-m dew point temperatures.

4.3. Sea Level Pressure Changes

Figure 4.4 shows little statistical significance in SLP for May except for the small region along the Louisiana-Mississippi border with difference values upwards of 0.1 hPa. In June,

B40C has wide regions of lower SLPs concentrated over the oil slick footprint (Figure 4.4B), consistent with its wide area of ubiquitous SST elevation maximized in June. The B40C model exhibits lower SLPs across most of the domain in July with the eastern portion of the GOM having differences exceeding –0.2 hPa. In both June and July, the southwestern corner of the domain features SLP differences closer to zero, which is expected given that the largest differences would likely be over the oil footprint (Figure 4.4E). In the GOM for August, the Louisiana and Mississippi coastlines show a statistically significant SLP difference approaching 0.1 hPa. Much of the differences where the oil slick footprint would be is considered statistically insignificant as the oil slick's SST increases have faded out by this time (Figure 3.5). Additionally, the Alabama and Florida area feature B40C SLP increases upwards of 0.1 hPa, and the southeastern quadrant of the domain maintains the slightly lower experimental SLPs that were seen in July. The summer for B40C's SLPs shows a similar trend to the T2s and TD2s. May starts out statistically weak but then the difference values grow into June coinciding with the increase in T2s. However, instead of the SLP differences in July growing closer to zero as the T2s did, B40C's SLPs decline and broaden across the domain before fading closer to zero along the central portion of the domain in August.

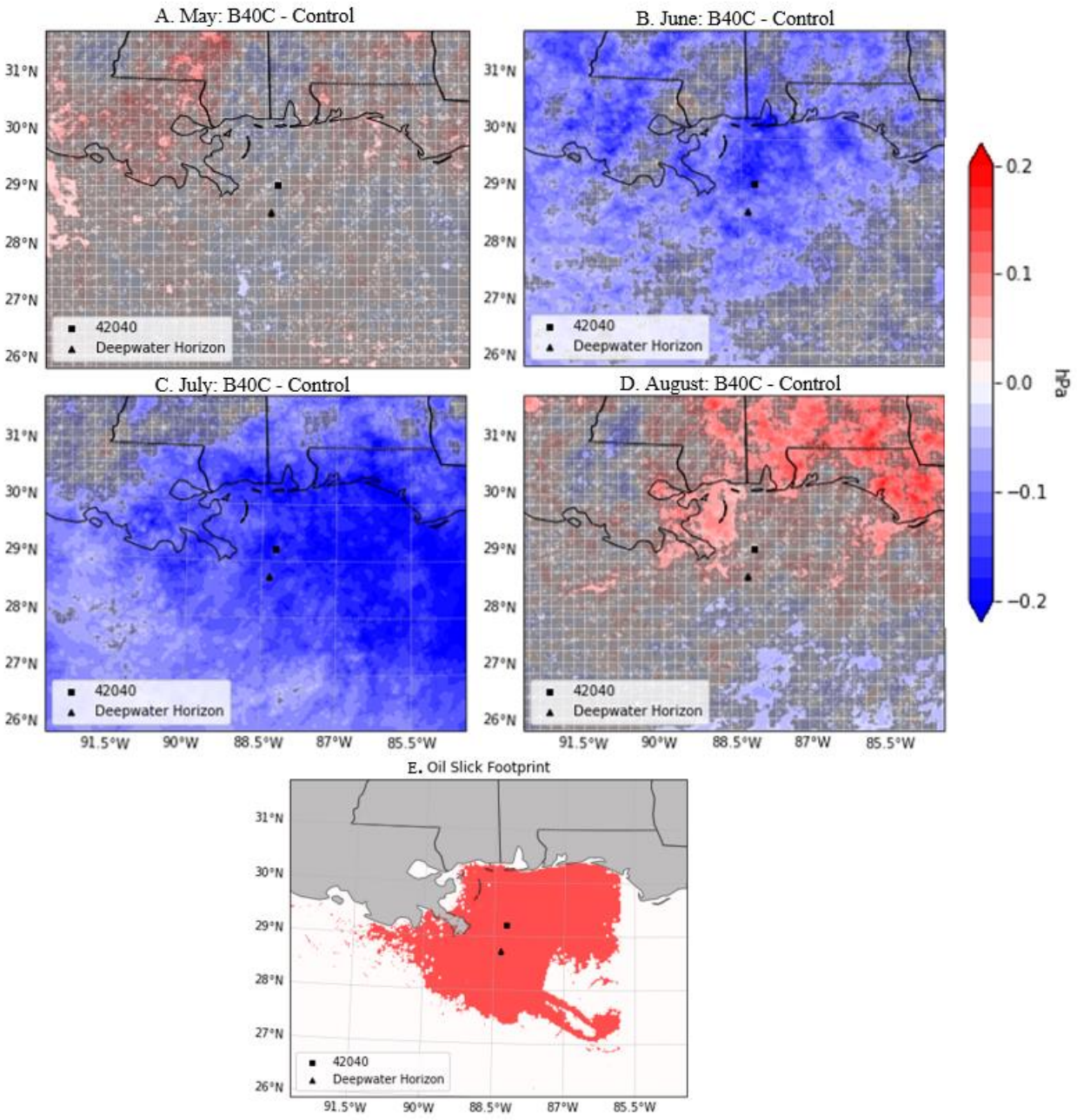

Figure 4.4. Same as Figure 4.2 except for SLP.

4.4. Response in Winds

The same method used to determine areas of statistical significance in the SLP was also used for the differences in wind speed (Figure 4.5). Theoretically, as the summer progresses there should be two main areas of wind-related interest: (1) the coastline where the land/sea

breeze cycle takes place; and (2) the highest-frequency portion of the oil spill frequency map (Figure 3.3). If the oil spill breaks down the sea breeze, then there should be a slowing of the average winds near the coastlines. The wind speeds may also strengthen around the oil slick as the pressure gradient is shifted due to changes in the SLP (Figure 4.4.). Examining the wind speed differences by month yields a general idea of important locations and trends in the models.

Within Figure 4.6, there is a discernable anti-cyclonic circulation and likely an offshoot of the Bermuda High (Cochrane & Kelly 1986) known to be an abnormally strong synoptic influence on 2010's summer (Miller & Mote 2017; NOAA 2011). The center of this circulation starts at the edge the domain in May (Figure 4.6A) and migrates farther westward as summer progress (Figure 4.6D), shifting coastal winds from a primarily south direction to a southwesterly direction over the oil slick (Walker et al. 1994, Walker et al. 2005).

June is the month when the oil footprint SSTs and T2s reach their maximum (Figures 4.2B and 4.3B) and similarly is the month when the wind speed differences reach their maximum of around 1 m s^{-1} (Figure 4.5B). When comparing against SLP in June (Figure 4.4B), the largest portion of statistically significant wind speed south of the Florida panhandle aligns with a relative maximum of –0.2 hPa difference in SLPs. Comparing these to the average wind direction for June (Figure 4.6B), wind flow in B40C comes from a more southerly angle than the control. Starting in June, the southwestern quadrant of the domain features sporadic areas of statistically significant higher control model wind speed, and although few points are considered statistically significant, this band of higher control model wind speed extends around the offshore coast of Louisiana and up into the Mississippi-Alabama border.

By July, the B40C wind speeds decline following the same northwest-to-southeast swath seen in the July T2s and TD2s previously (Figures 4.2C and 4.3C). Additionally, there is a

lateral swath of wind speed differences between 0 and –1.5 m s^{-1} along the GOM coastline, which was hypothesized in Figure 2.1. July for B40C does contain a region of faster winds than the control model south of the Florida panhandle. This region east of DWH and Buoy 42040 is also where SLP differences for July were almost ubiquitously beyond – 0.2 hPa (Figure 4.4C), and the wind directions for July (Figure 4.6C) are coming from an east-southeast direction. Together these create a rectangular region of faster winds heading toward the DWH and Buoy 42040. In August, there is a distinct lack of statistical significance, with the only areas of higher B40C wind speeds in the southern region of the domain. Because the SLP for B40C was higher than the control over Florida and Alabama (Figure 4.4D), the slower, southwesterly winds are likely due to trying to push against the resulting pressure gradient.

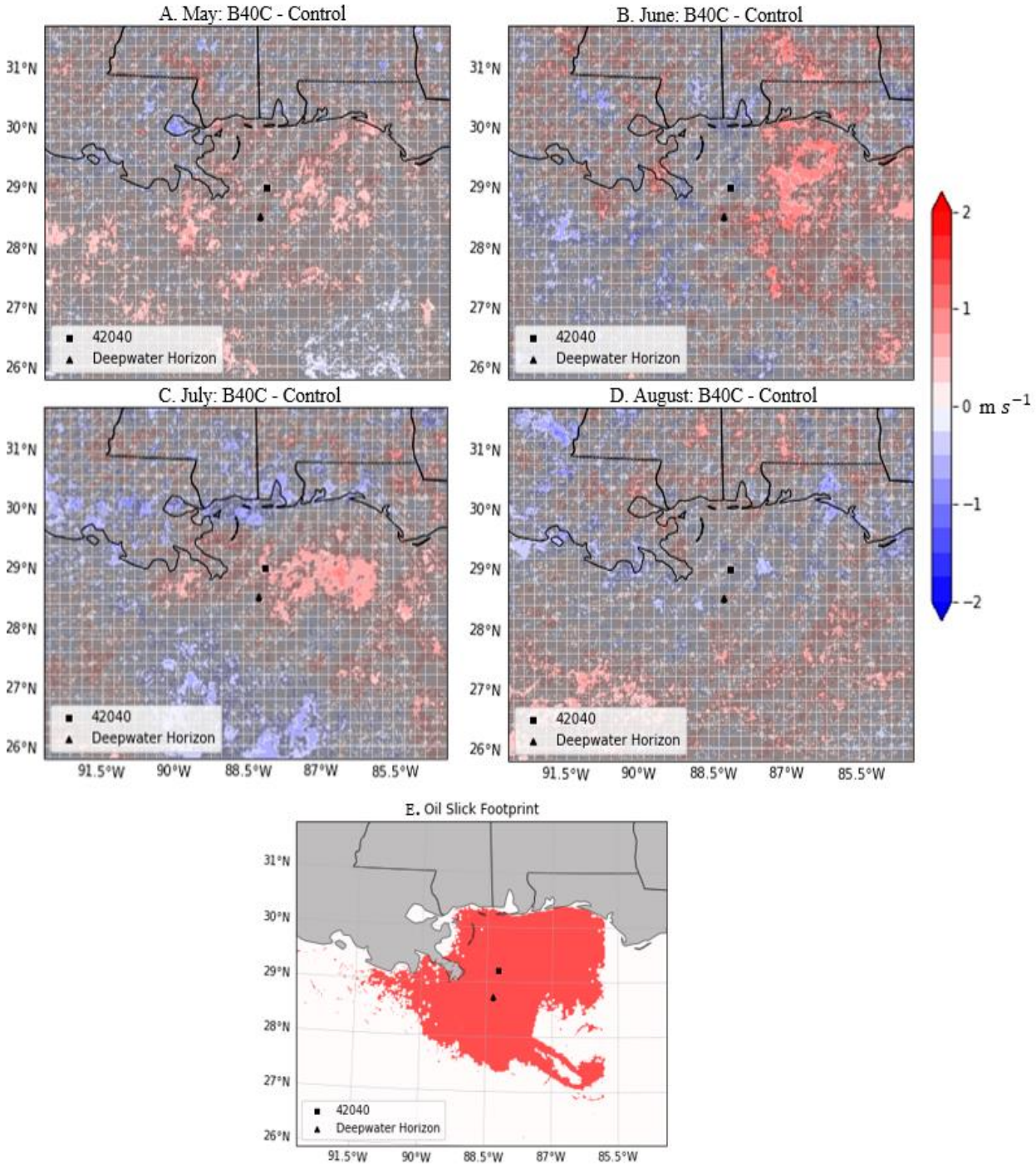

Figure 4.5. Same as Figure 4.2 except for wind speed.

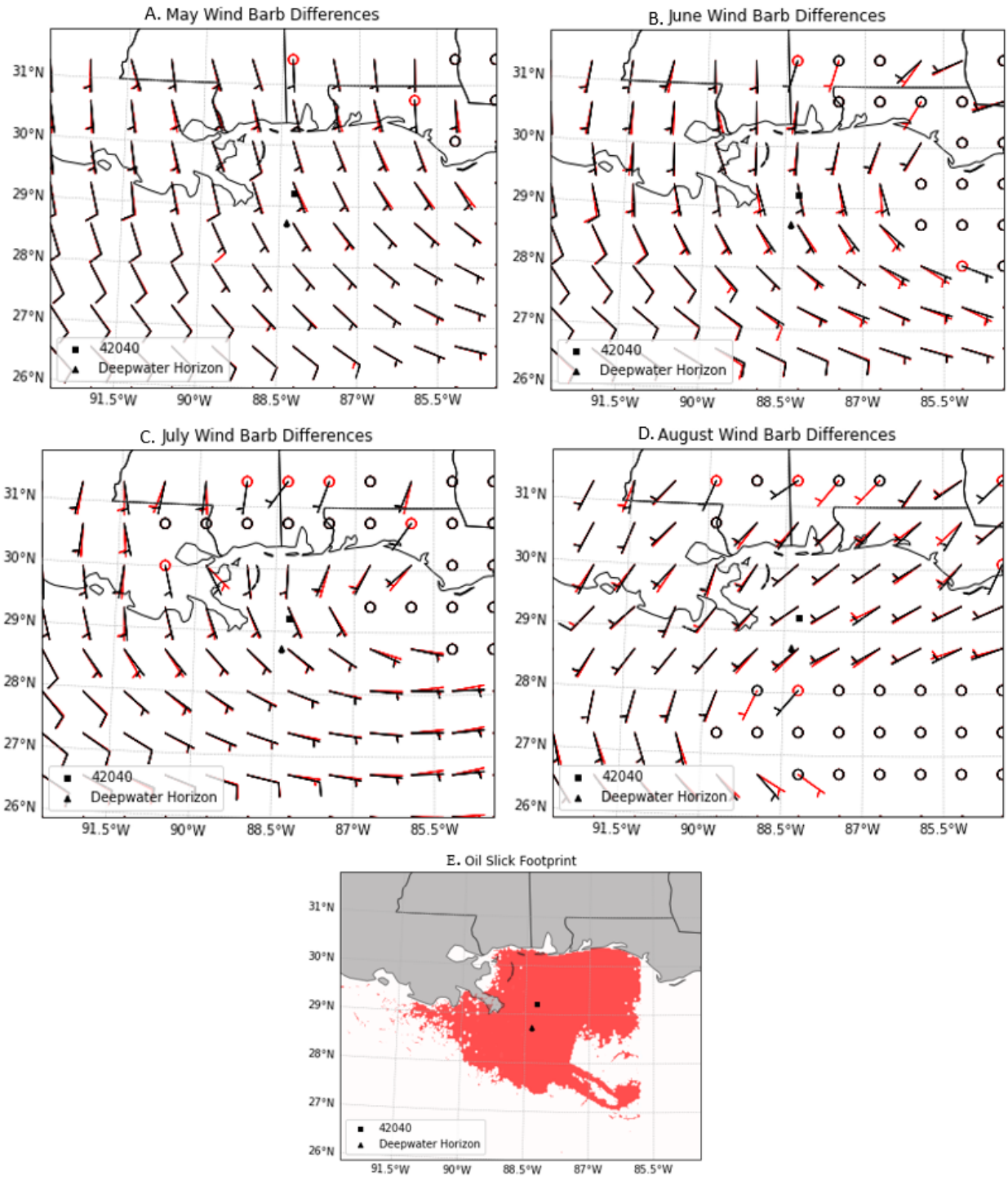

Figure 4.6. Same as Figure 4.2 except for wind direction. Red wind barbs indicate B40C and black wind barbs indicate the control simulation.

4.5. Cloud Fraction and Precipitation

For the month of June, Figure 4.7A-C shows that across most of the oil slick footprint, there were lower percentages of cloud fraction for low, medium, and high levels in B40C versus the control. While these differences were largely insignificant in the lower levels, roughly the same area from the tip of Louisiana to Alabama shows statistically significant difference values less than –2.5% for both the medium and high levels. At medium and high levels, the southeastern region of the domain features positive cloud fraction difference values exceeding 5% indicating that at higher levels the experimental model is resolving more cloud coverage in that corner.

July's cloud fractions strongly contrast with those of June (Figure 4.7D-F). At the low and medium levels, B40C exhibits higher cloud fractions in the northern, central GOM where the oil footprint reaches the coastline. The medium and high levels show a large statistically significant swath extending from the Louisiana coast to the southeast corner of the domain with difference values exceeding 5% where B40C has a higher cloud fraction. At the low level, however, this same zone is dominated by negative difference values, suggesting B40C generates fewer clouds in this layer, though the differences are statistically insignificant.

The average lifted condensation level (LCL) height difference for July is plotted in Figure 4.8. When compared against the mean low-level cloud fraction for July (Figure 4.7D), the region of the lesser B40C cloud fraction aligns with the higher LCL heights for B40C in Figure 4.8. B40C was, on average over the month, resolving clouds over this area at a higher altitude than in the control model, which corresponds to the increases in medium and high-level B40C cloud fraction in July. Additional evidence of this comes from the T2s and TD2s (Figures 4.2C and 4.3C). In the same areas, the greater dew point depression (i.e., lower TD2s and higher T2s) for B40C would mean that an air parcel rising would require greater vertical ascent to reach saturation

than it would in the control model. August is when B40C's oil footprint SSTs decline back to being non-elevated and cloud fractions across all height levels begin to look similar to the control model. Cloud fraction for B40C maintains the pattern seen in the other variables of interest, whereby the elevated oil slick footprint SSTs peak in June, but the model impacts are most noticeable in July and then taper off in August.

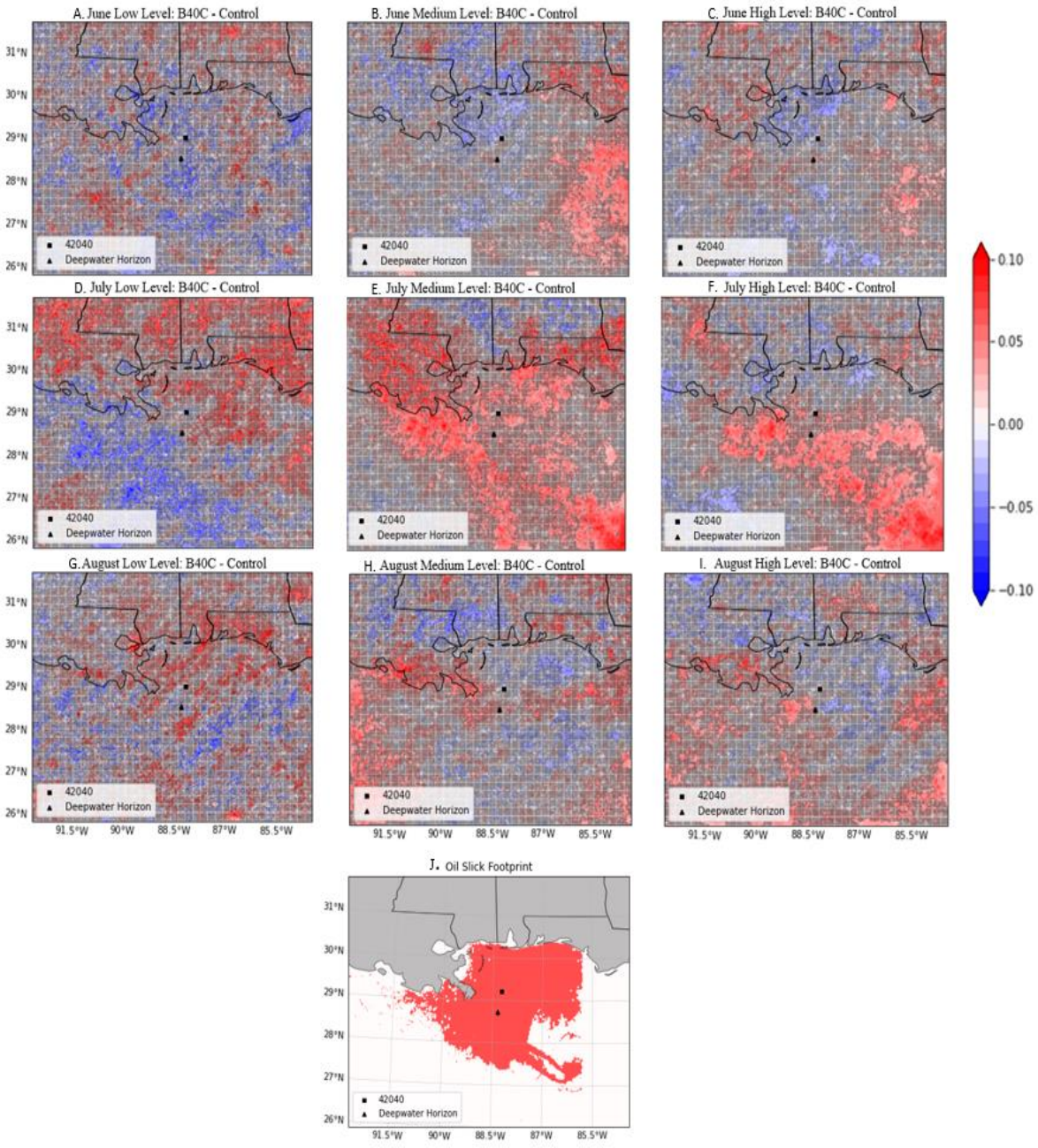

Figure 4.7. A-I) Average June, July, and August cloud fraction differences of B40C minus the control model where red indicates lesser quantities of clouds and blue indicates greater. Stippled areas indicate statistical insignificance with a 95% confidence. J) Oil slick footprint outline.

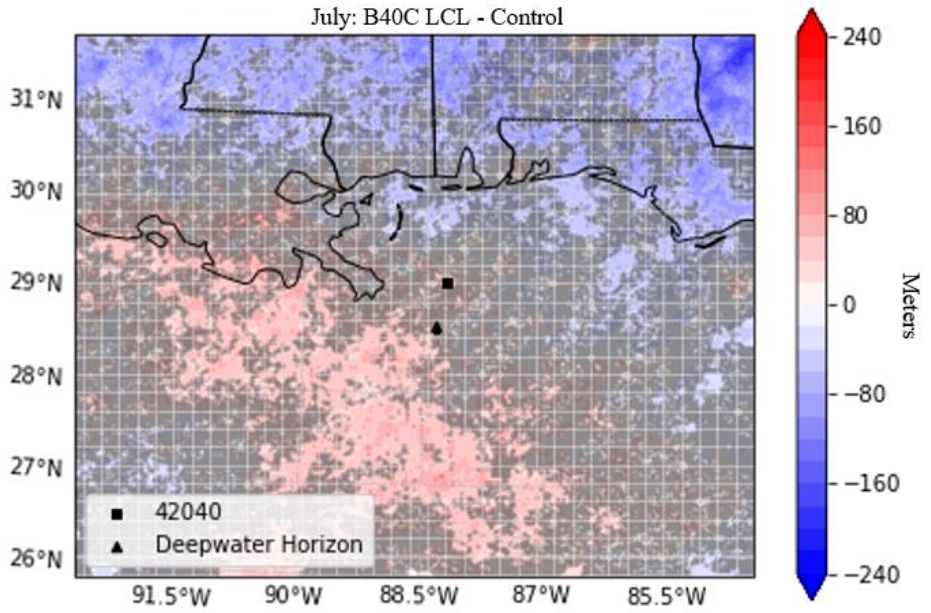

Figure 4.8. Mean July LCL height difference of B40C minus the control where blue indicates higher control values and red indicates higher experimental values. Statistical significance with a 95% confidence interval is non-greyed on the plot.

For May through August, precipitation for both B40C and the control model significantly underperformed when compared to the observed precipitation in Figure 4.9A. The scenarios' precipitation peaked at around 800 mm, whereas the observed precipitation from the combined IMERGS microwave-IR estimation accumulated about 1300 mm. Both the control and B40C scenarios resolve most precipitation onshore whereas the IMERG data places the maximum regions of precipitation over the GOM and clustered near the coastline. Within the boxed zone of interest (1) of Figures 4.9C and 4.9D, both models are trying to resolve similarly located precipitation; however, the control model generates higher quantities. This can also be seen in the boxed zone of interest (2). The boxed zone of interest (3) however depicts the opposite, where B40C places a higher quantity of precipitation. When examining the offshore precipitation in Figure 4.9C, B40C features more rainfall over the offshore area of the domain. Another location of model agreement is indicated by the black arrow in Figures 4.9A, 4.9C, and 4.9D.

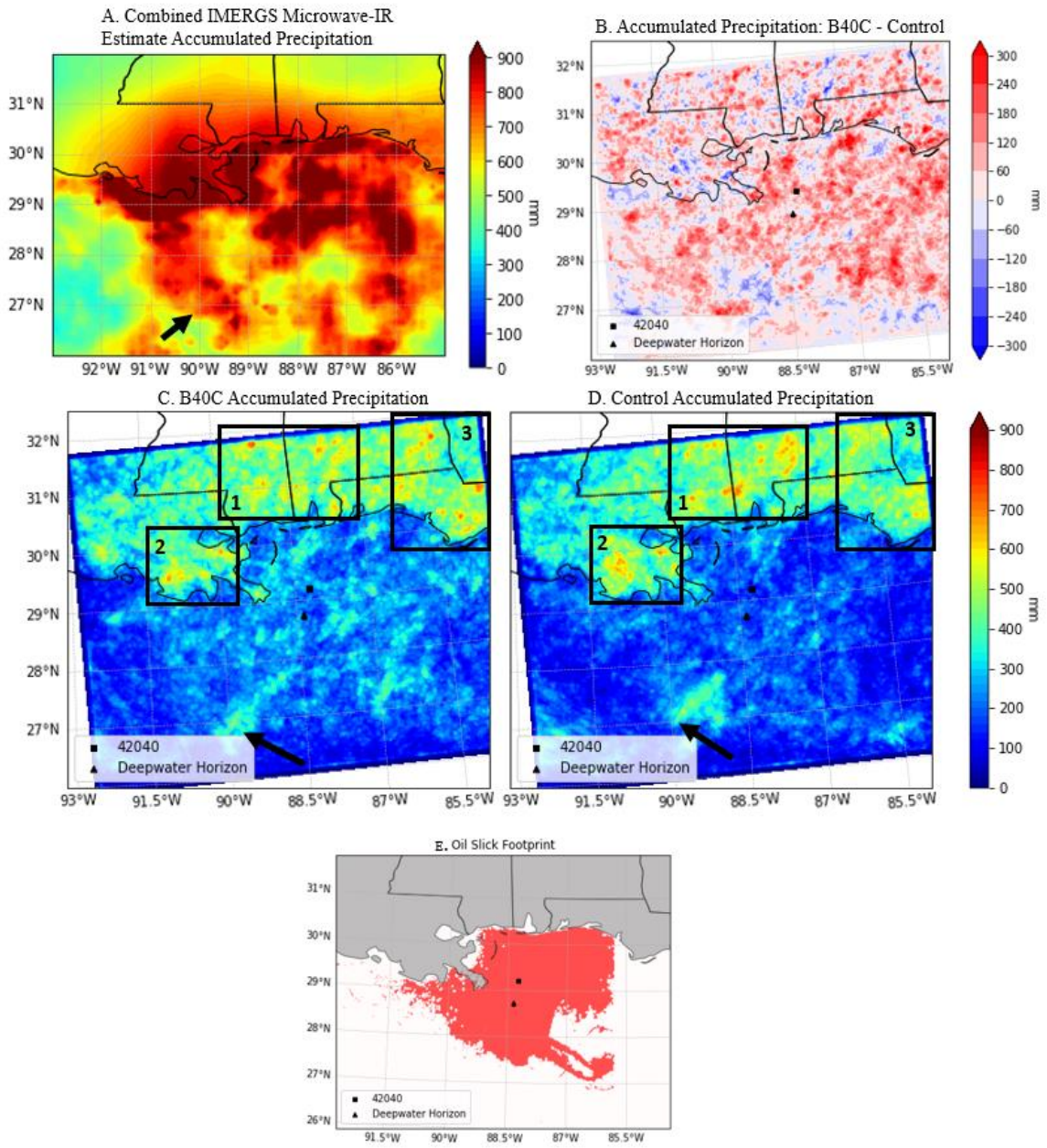

Figure 4.9. A) IMERG observed precipitation in millimeters. B) Differences in accumulated precipitation of B40C minus the control model where red indicates higher B40C precipitation and blue indicates higher control precipitation. C) and D) Total precipitation from the B40C and control scenarios respectively. The outlined box 1 – 3 indicates a zone of interest and the arrow indicates another point of interest. E) The oil slick footprint outline.

Although the precipitation did underperform, important spatial and temporal information can still be gleaned from the models. Figure 4.10 contains the accumulated precipitation for B40C, the control model, and the observed monthly data. The difference in average daily

precipitation is also accounted for (Figure 4.10 J-L). For both simulations, the precipitation comes most often in June (Figures 4.10A and 4.10D) whereas in the observed data the maximum precipitation is in August (Figure 4.10I). Few places were considered statistically significant in June or July between the differences in daily averaged precipitation, but overall precipitation for B40C was in greater quantity and features some small regions of statistical significance marked by the black arrows labeled "1" and "2" in Figures 4.10J and 4.10K respectively. In June, the observed precipitation shows a large segment of rainfall along the Louisiana coast and in the southwestern quadrant of the domain as indicated by the black labeled arrows "3" (Figure 4.10G and 4.10J). At these same locations, B40C and the control model both seem to try to resolve this feature, but the control model does so marginally more successfully. Neither successfully modeled the precipitation surrounding the *Deepwater Horizon* in June (Figure 4.10G). As indicated by the black arrow labeled "4" in Figure 4.10H, July brings an area of precipitation in the observed data of around 400mm. This is not mirrored exactly in the simulations, but B40C does have an area of higher precipitation structurally similar and near the same region (Labeled as the black arrow "4" in Figure 4.10K). The simulations look nearly identical in August with neither presenting nearly the quantity of rainfall that the observed data shows in Figure 4.10I. This is most likely due to the elevated SSTs over the oil slick footprint being decreased to zero in August as seen in 3.5. For B40C, many variables manifested at their strongest and most consistent in the month of July. This was seen in the TD2s (Figure 4.3), SLPs (Figure 4.4), wind speeds (Figure 4.5), LCL height (Figure 4.8) and cloud fraction (Figure 4.7). However, precipitation was most accumulated in June for both models. The disparity between the models' precipitation and the observed could be a result of different factors including influence from

parameterization schemes or microphysics adjustments as well as WRF not capturing a potentially important synoptic scale event.

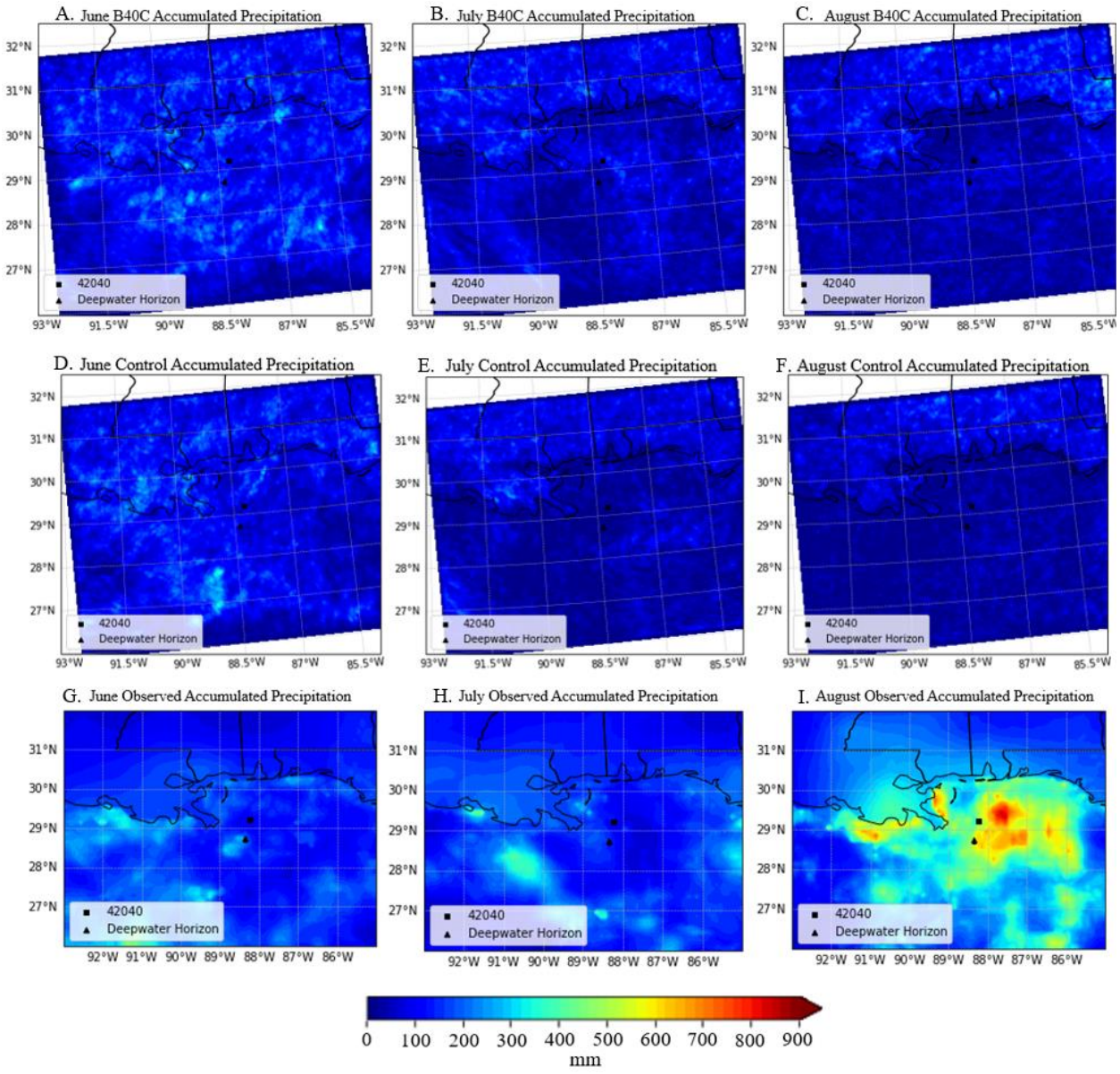

Figure 4.10. A-C) B40C accumulated precipitation for the months of June, July, and August respectively. D-F) Control model accumulated precipitation for the same time frame. G-I) Observed IMERG accumulated precipitation for the same time frame. J-L) Mean daily difference for precipitation for each month with B40C minus the control. Red indicates greater B40C precipitation and blue indicates greater control model precipitation. Stippled areas indicate statistical insignificance with a 95% confidence in J-L. A-L are all plotted in mm. M) Oil slick footprint outline. The black arrows indicate areas of interest.

Figure Continued.

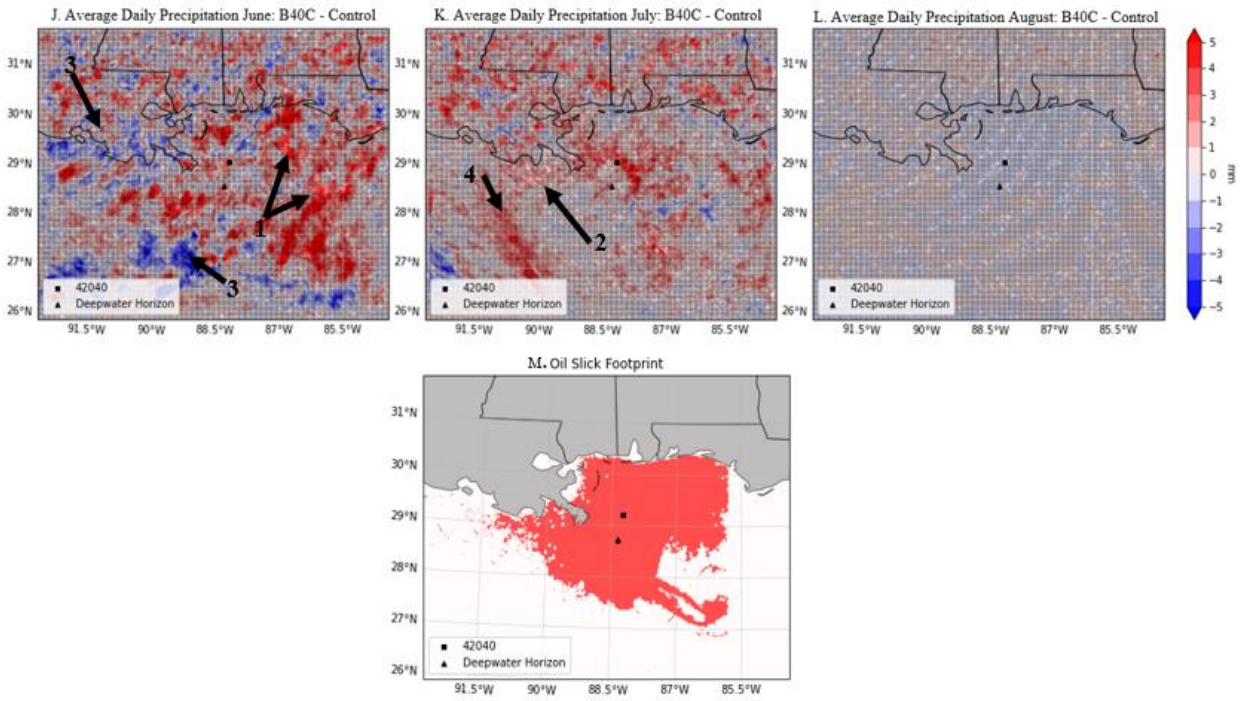

4.6. Sensitivity to the SSTs in WRF Models.

4.6.1. Decay Scenario Impacts to 2-m Temperatures and 2-m Dewpoint Temperatures

In addition to the primary model B40C, three other simulations (B40D, B40ED, and A40D) were run in order to determine the sensitivity of the model based on differing levels of SST elevation. Information regarding these three scenarios can be found in Table 3.3. Each scenario had a maximum elevation at the highest frequency portion of the frequency map and each lower frequency had a lowered SST to correspond until the frequency equaled zero. B40ED featured the highest SST elevation in the highest frequency portion of the map at 1.909 C°, B40D had the next highest at 0.437 C°, and A40D had the lowest at 0.300C°. The response in T2s to each scenario's respective SST elevation can be seen in Figure 4.11, where B40ED has the highest and most defined response to the SSTs followed by B40D then A40D with a smaller response. Some patterns emerge between these scenarios, however. In July (Figures 4.11B, 4.11E, 4.11H, and 4.11K), each scenario exhibits a strong increase in experimental T2s

southwest of Lake Pontchartrain. At the same time in the southern portion of the domain, statistically significant difference values between 0.0 C° to – 0.4 C° indicate the control model was warmer across the swath indicated by the black arrow labeled "1." In August, the T2s over the oil slick footprint are similar to the control scenario, but B40ED still shows some statistically significant regions of higher experimental model T2s south of the Louisiana coastline (Figure 4.11F indicated by the black arrow labeled "2") absent in B40D or A40D. Each of these three models includes a zone of higher control model temperatures just off the Florida coastline, and each model also has higher experimental T2s over the Mississippi-Louisiana border indicated by the black labeled arrow "3" in Figures 4.11C, 4.11F, 4.11I, and 4.11L. This area is most expansive in B40ED and least expansive in A40D and B40C.

In comparison to B40C's T2s (Figure 4.11J-L), the patterns noted in this section are noticeable in that model as well. In June, in B40C shows the same lower T2 difference values over the Mississippi-Alabama border that each of the other models shows (Figures 4.11B, 4.11E, 4.11H, and 4.11K indicated by the arrow labeled "4") with B40ED and B40C displaying it most prominently. B40C also displays the same lower T2s across the southern portion of the domain in July (Figures 4.11B, 4.11E, 4.11H, and 4.11K indicated by the black arrow labeled "1") and shows the same increase in experimental T2s southwest of Lake Pontchartrain. August for B40C appears similar to the other models where the Mississippi-Louisiana border has greater statistically significant values of experimental temperatures than the control.

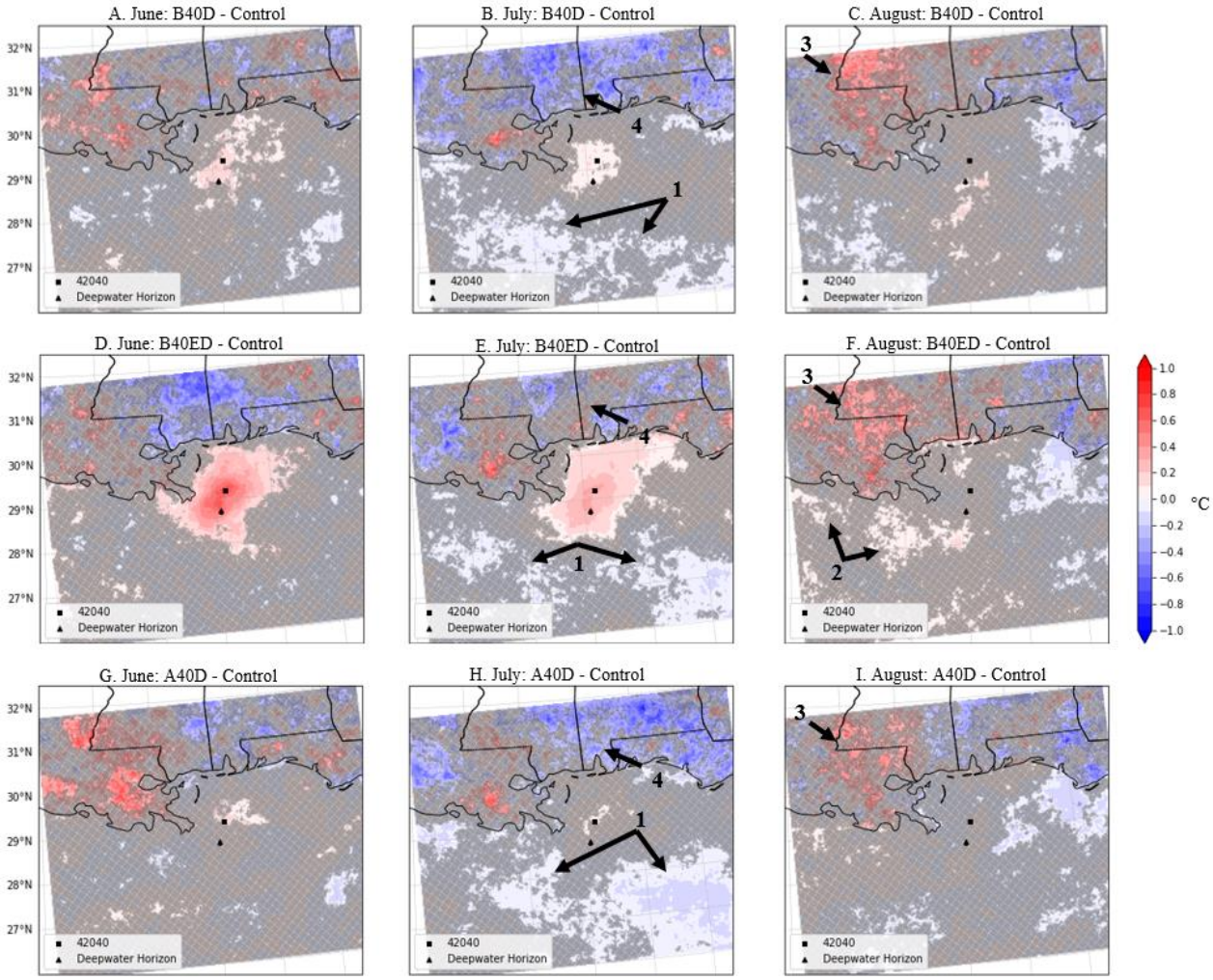

Figure 4.11. A-L) June, July, and August mean T2 differences for experimental models minus the control, where blue values indicate higher control T2s and red indicates higher experimental T2s. Stippled areas indicate statistical insignificance with 95% confidence. M) Oil slick footprint outline. The black arrows indicate areas of interest.

Figure Continued.

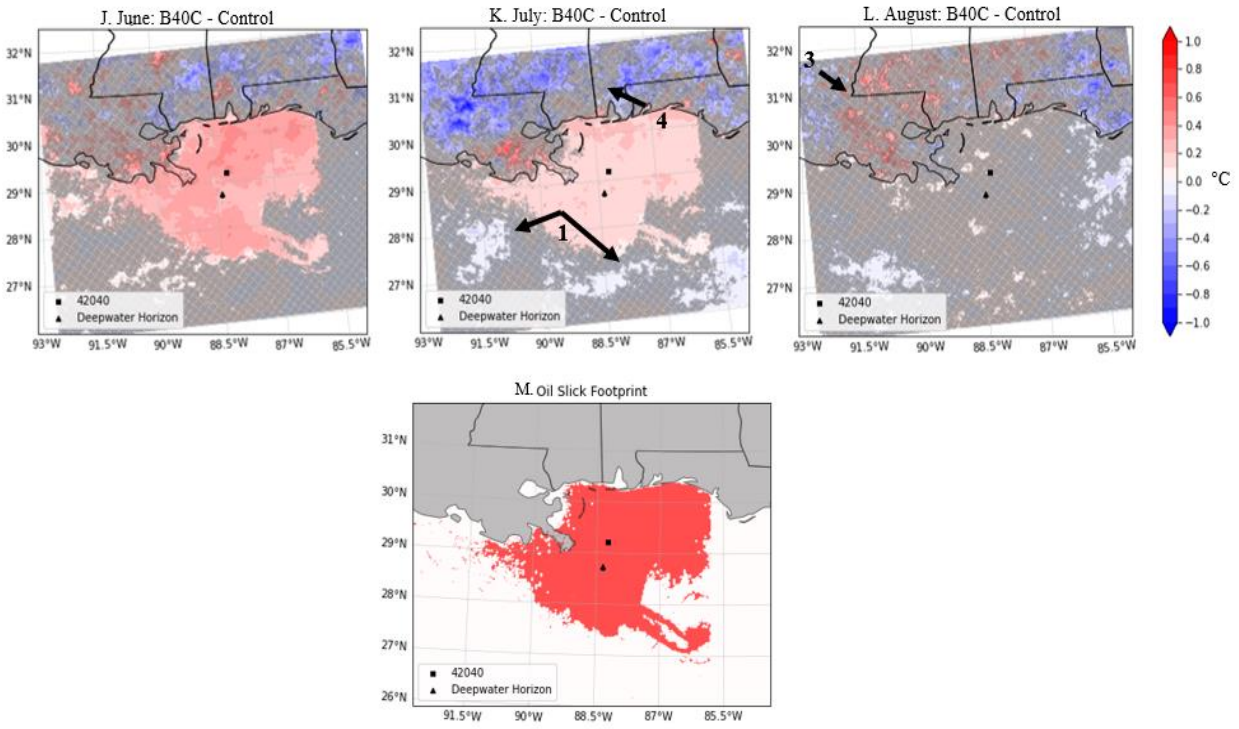

Examining the response in TD2s for the decay models (B40D, B40ED, and A40D) (Figure 4.12) again shows similarities when compared to the B40C TD2s. For June, B40D and B40ED both show statistically significant areas of difference values exceeding 0.25 C° concentrated on the highest region of frequency around DWH (Figures 4.12A and 4.12D). The ubiquitous SST elevation in B40C exhibits a similar response seen in Figure 4.12J but is more widespread across the general outline of the footprint. B40ED has a region of lower TD2s than the control model indicated by the black labeled arrow "1" in Figure 4.12D. B40C presents the same lower TD2s in the same location (Figure 4.12J indicated by the arrow labeled "1"). Additionally, both B40C and the decay models, include the same region of lower experimental TD2s over Florida indicated by the black arrow labeled "2" in Figures 4.12A, 4.12D, 4.12G, and 4.12J.

In July, following the same swath of lower decay scenario July T2s in Figure 4.11, there is a statistically significant region of lower TD2s in the decay scenarios (labeled “3” with the black arrows in Figures 4.12B, 4.12E, 4.12H, and 4.12K). This pattern was seen in the comparison of B40C to the control model as well, but B40C also had a stronger TD2 presence just south of the Florida panhandle that is not reproduced in the decay scenarios. At the point indicated by the black labeled arrow “4” in Figures 4.12B and 4.12E, B40D and B40ED both have TD2 values around 0.5 C° cooler than the control. This is the same location where there are lower experimental July T2s versus the control (Figure 4.11).

With August, as the elevated SSTs decrease back down to zero, the experimental scenarios begin to trend towards fewer differences between the control. However, each of the experimental scenarios, including B40C, shows a region of lower TD2s south of the Florida panhandle (Figures 4.12C, 4.12F, 4.12I, and 4.12L), and each, except B40ED, shows lower experimental TD2s along the Louisiana coastline. Another feature present in all scenarios for August is the zone of higher experimental TD2s indicated by the black arrows labeled “5” in Figures 4.12C, 4.12F, 4.12I, and 4.12L. This region of statistically significant positive difference values follows northeastward through Lake Pontchartrain and then widens out to cover most of the onshore portion of the domain.

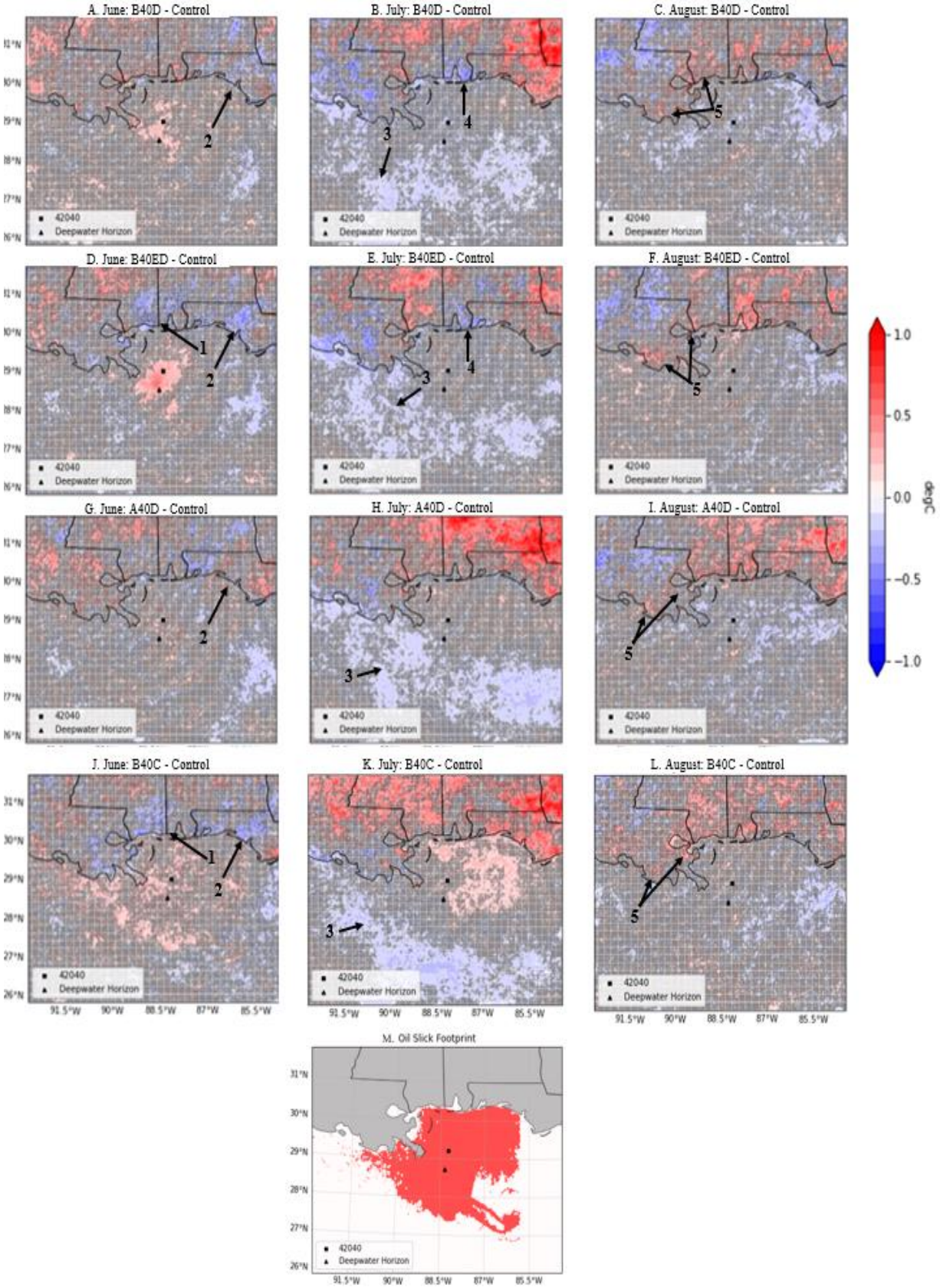

Figure 4.12. Same as Figure 4.11 except for TD2.

4.6.2. Changes in Decay Scenario SLP

Figure 4.13 contains the differences between the decay scenarios and the control SLP for June through August. While B40C had significantly lower SLPs, compared to the control, across the domain for June and July (Figure 4.13J-K), the decay scenarios largely feature lower SLPs than the control but more sporadic for B40D and B40ED in June (Figures 4.13A and 4.13D). In July these lower SLPs start to expand across the GOM for B40D and B40ED (Figure 4.13B and 4.13E). B40D especially shows lower SLPs around the coastline and along the edges of the domain while B40ED exhibits a pattern similar to B40C of dominating the entirety of the GOM, although B40ED does include a region of maximized lower pressures near DWH and Buoy 42040. For each of the models in August (Figures 4.13C, 4.13F, 4.13I, and 4.13L), there are large regions of positive difference values, where the experimental models have higher SLPs than the control, over the Alabama-Florida region. For all the decay models except B40ED, this region of positive difference values extends southwestwards along the Louisiana-Mississippi coastline.

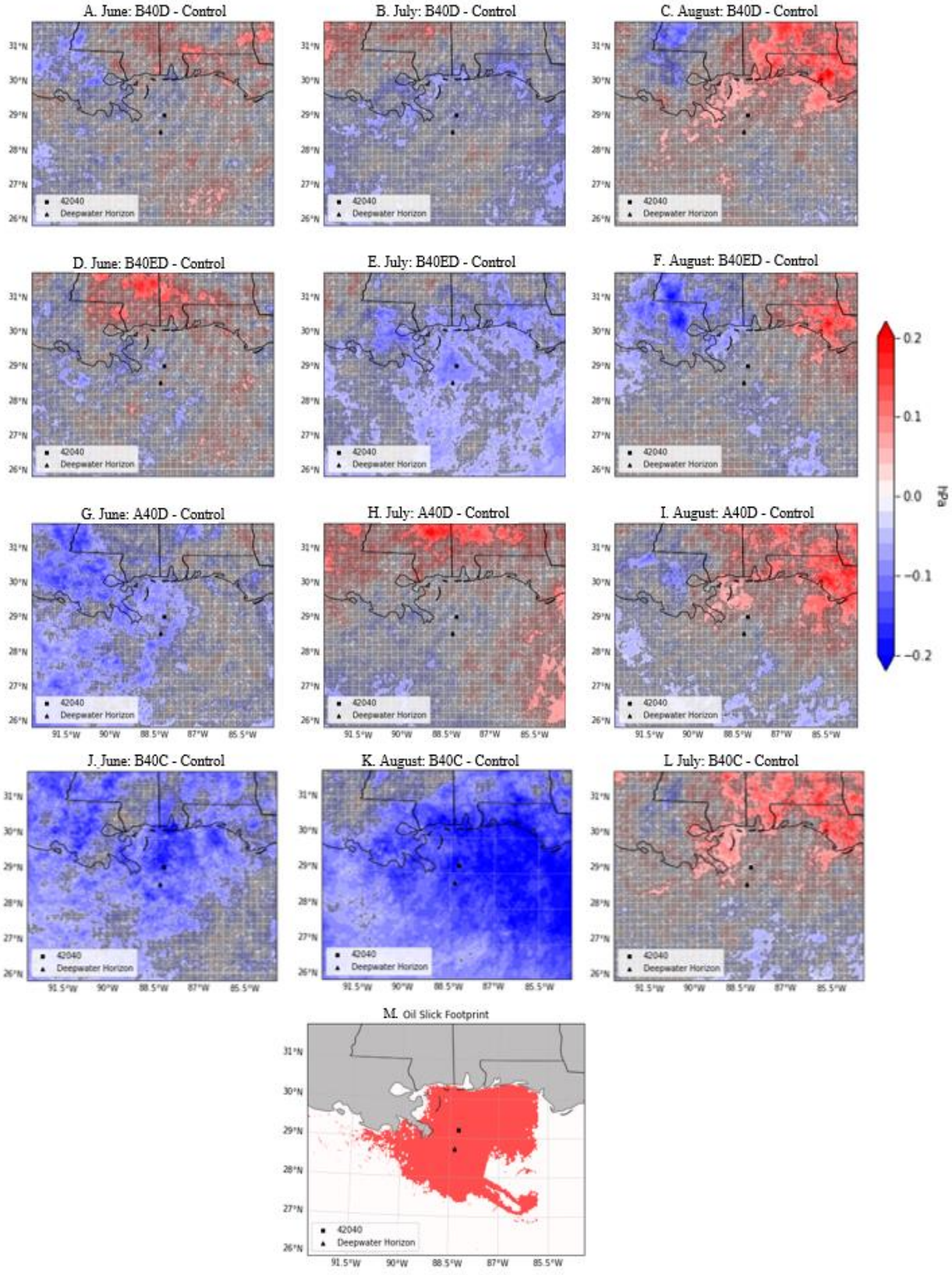

Figure 4.13. Same as Figure 4.11 except for SLP.

4.6.3. Response in Decay Scenario Wind Speeds

Average wind speed differences between the decay scenarios and the control across the months of June through August are plotted in Figure 4.14. Across all experimental scenarios are statistically significant higher wind speeds than the control along the Louisiana coastline in June (Figures 4.14A, 4.14D, 4.14G, and 4.14J indicated by the black arrows labeled "1"). Both B40D and B40ED show a small area of faster wind speeds over Lake Pontchartrain with B40ED being slightly larger and with higher values (Figures 4.14A and 4.14D). In June also, each of the experimental scenarios has a region of slower wind speeds along the Mississippi-Alabama border at the arrow labeled "2;" however, this region is considered statistically significant only in B40ED and B40C (Figures 4.14D and 4.14J). The large section of higher B40C wind speeds south of Florida in Figure 4.14J is absent in any of the other experimental scenarios.

July is when most of the scenario variation seems to take place in the wind speeds. Figure 4.14 B shows B40D having faster wind speeds in a northwest to southeastern diagonal line while B40ED (Figure 4.14E) shows a similar area, but farther north and with a maximum near the DWH and Buoy 42040. Although statistically insignificant for most of the scenarios, July also features a belt of slower experimental wind speeds along the 30°N latitude line indicated by the black arrow labeled "3" in Figures 4.14B, 4.14E, 4.14H, and 4.14K with this phenomenon is most clear in B40D and B40C.

For August, the scenarios again show more variation for wind speed than they did for the previous variables. B40D places slower winds over DWH and buoy 42040 (Figure 4.14C). This is somewhat echoed in A40D but to a lesser extent and not evident in B40ED. All the decay scenarios feature faster wind speeds in Louisiana west of Lake Pontchartrain (Figures 4.14C, 4.14F, and 4.14I), but this is not evident in B40C. The boxes labeled "A" in Figures 4.14C,

4.14F B40D and B40ED show a region of increased wind speed, and this is mirrored in B40C as well (Figure 4.14L). It is not seen in A40D, however. Additionally, in each experimental scenario, there is a region of slower wind speeds along Florida's panhandle indicated by the arrow labeled "4" (Figures 4.14C, 4.14F, 4.14I, and 4.14L), but this pattern is poorly aligned in each scenario with B40D representing it least significantly and A40D resolving the pattern farther north.

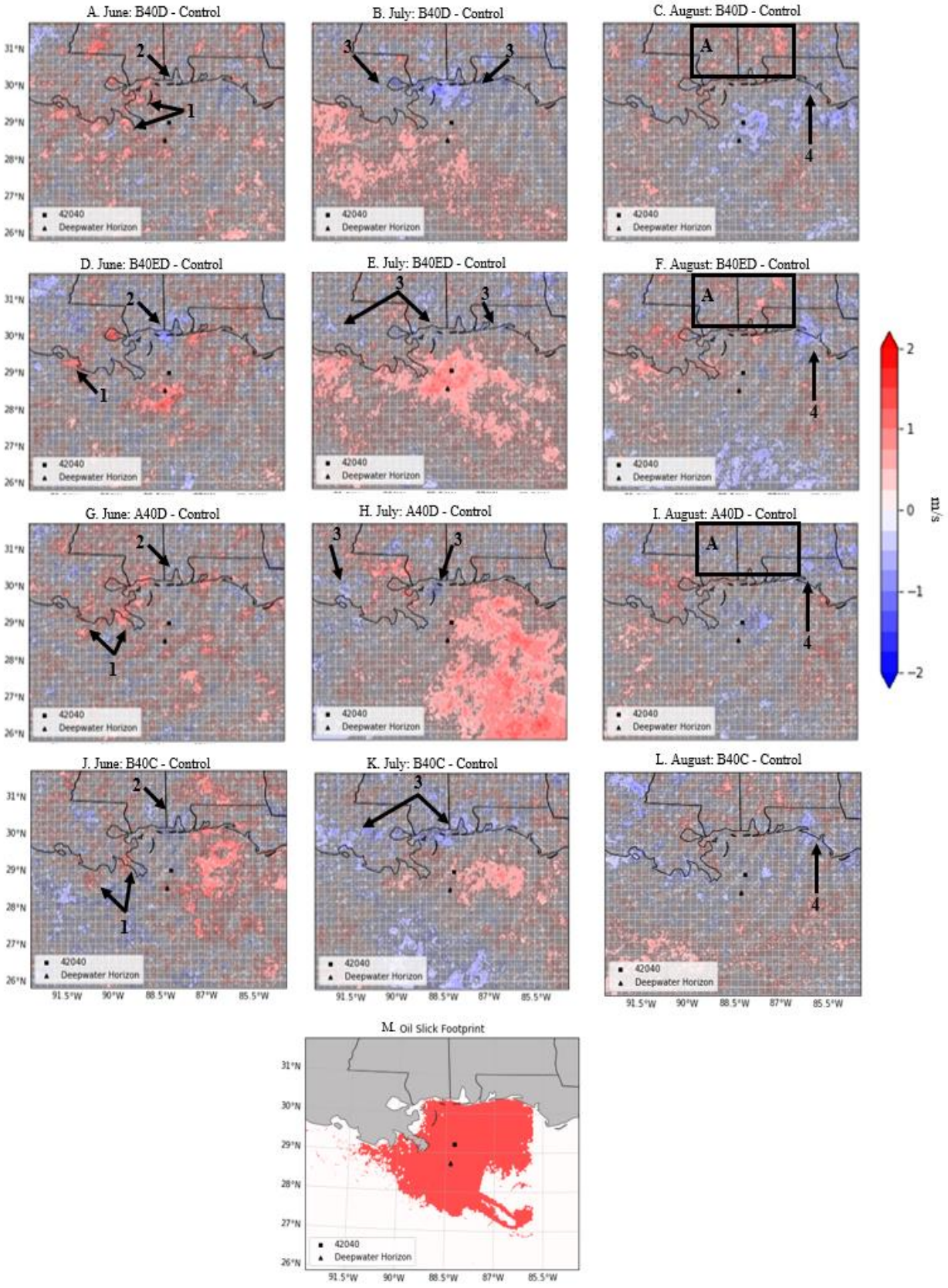

Figure 4.14. Same as Figure 4.11 except for wind speed.

4.6.4. Changes in Decay Scenario Cloud Fraction and Precipitation

July low, middle, and high-level cloud fractions are plotted in Figure 4.15. Analogous maps for May, June, and August are not shown, as most values were insignificant. The low-level cloud fractions were largely insignificant (Figures 4.15A, 4.15D, 4.15G, and 4.15J); however, they do show a recurring pattern that was manifested in B40C's low-level cloud fractions: the diminished cloud fraction values indicated by the black arrows labeled "1" which aligns with the lower experimental T2s and TD2s in Figures 4.11 and 4.12, respectively. The middle levels (Figures 4.15B, 4.15E, 4.15H, and 4.15K) show a consistent pattern across all the decay scenarios where there is a large zone of higher experimental cloud fractions that extends diagonally across the domain. The same pattern was seen in B40C's middle-level cloud fraction, but B40C's featured much wider spread values of middle-level cloud fractions similar to what is seen in A40D. The high-level cloud fraction shows that in most of the experimental scenarios, significant cloud fraction differences occur over the domain ocean and less so over land with A40D being the exception. High-level cloud fractions for B40D and B40ED (Figures 4.15C and 4.15F) mimic the middle-level cloud fractions similar to B40C (Figure 4.15L). Additionally in the high-level cloud fractions, on the coastline where Mississippi meets Alabama (indicated by the arrow labeled "2"), there is a small region of lower cloud fraction in each experimental scenario not seen at the lower levels.

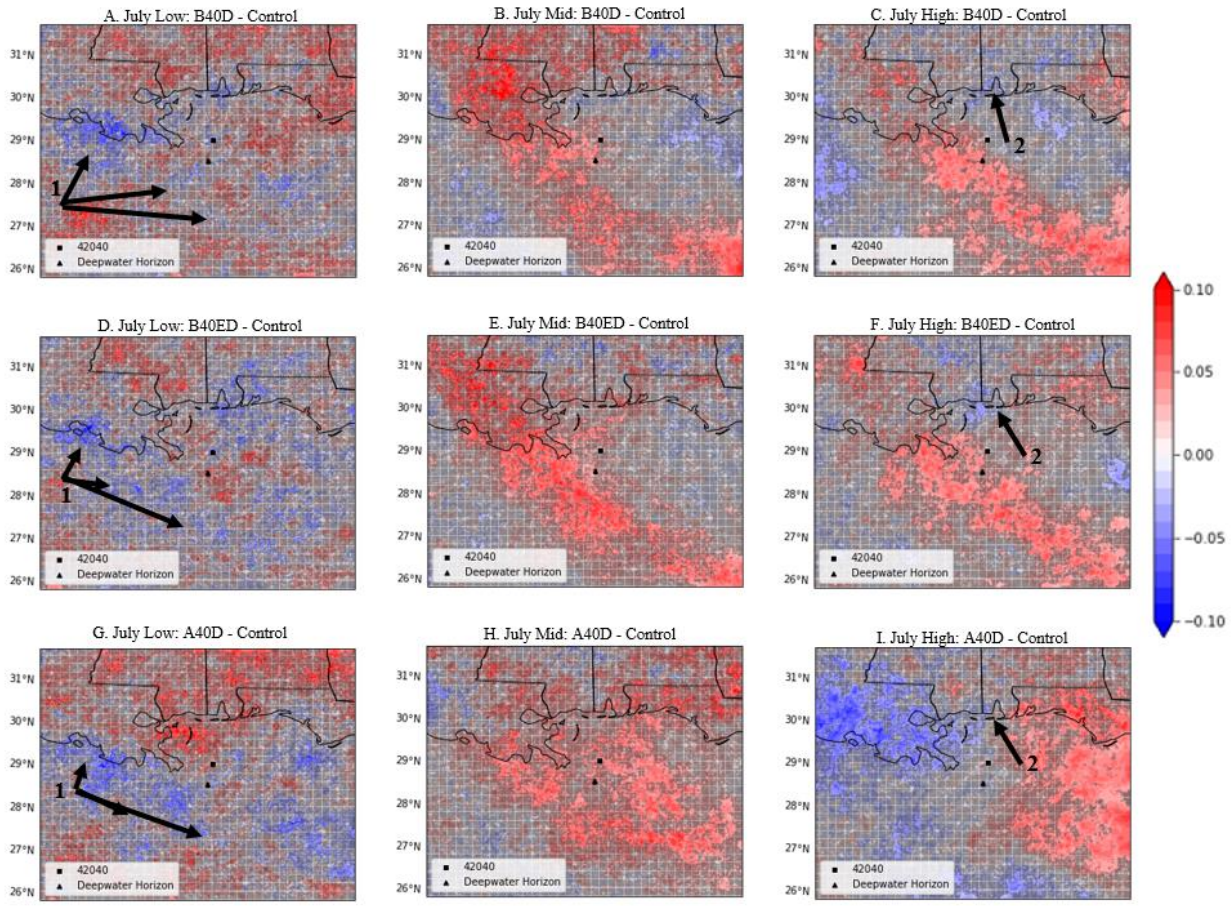

Figure 4.15. A-C) B40D July mean low, middle, and high-level cloud fraction differences for experimental scenario minus the control. D-F) Same as A-C) but for B40ED. G-I) Same as A-C) but for A40D. J-L) Same as A-C) but for B40C. Blue values indicate higher control cloud fraction and red indicates higher experimental cloud fraction. Stippled areas indicate statistical insignificance with 95% confidence. M) is the oil slick footprint outline. The black arrows indicate areas of interest.

Figure Continued.

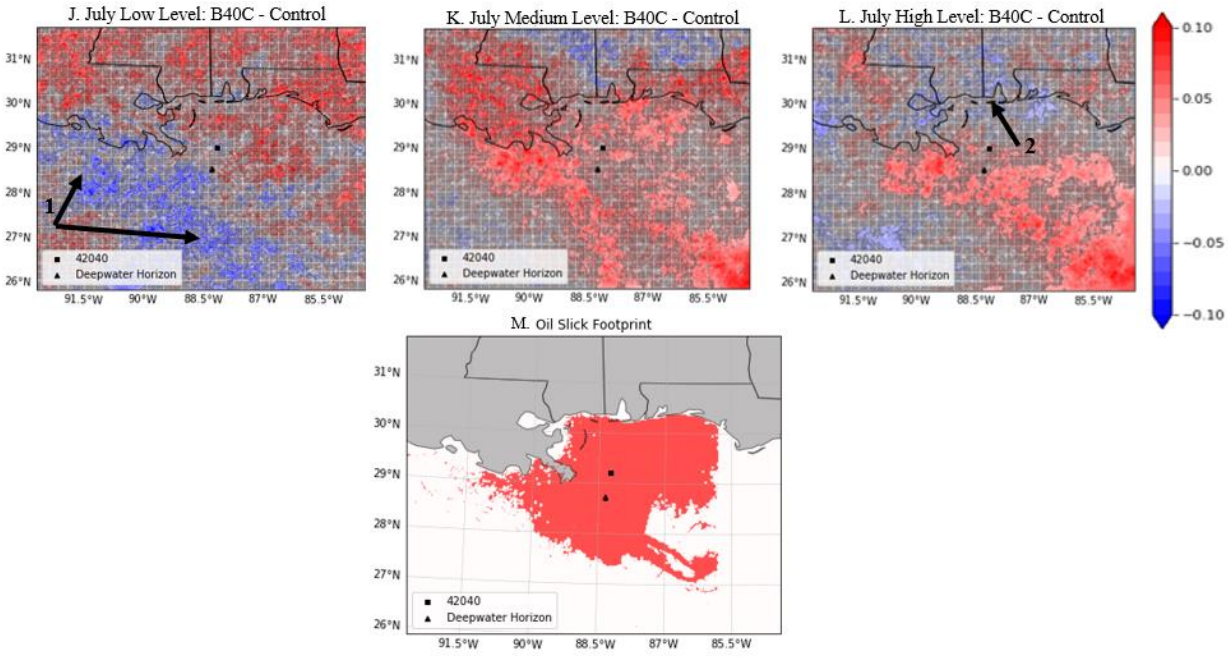

While there are few statistically significant areas for the decay scenario's daily averaged precipitation by month, the key features are the spatial patterns that arise from each simulation. Similar to B40C the bulk of the precipitation for each scenario came in June with a moderate amount in July and almost none in August except for B40D (Figure 4.16). For June, B40D and A40D place most of their precipitation south of the southeast Louisiana coast whereas B40ED places it in more centralized in the domain (Figures 4.16A-B, I-J). In comparison, B40C is the only scenario that places a large quantity of precipitation in the eastern portion of the domain (Figure 4.16J). In each experimental scenario, there is a small zone of lower precipitation indicated by the arrow labeled "1" that exists around the edge of Mississippi into Alabama (Figures 4.16A-B,I-J).

July is when less precipitation occurs in B40D and B40ED, but both display a swath of increased precipitation indicated by the arrow labeled "2" (Figures 4.16C and 4.16D). This same feature was seen in B40C's July daily average precipitation (Figure 4.16L), and all experimental

scenarios include a small region of decreased precipitation along the Mississippi-Alabama coastline (indicated in Figures 4.16C-D, K-L by the arrow labeled ”3”) that, while not considered statistically significant, appears in each scenario. The accumulated precipitation for each of the decay scenarios yields some locations of commonality (Figures 4.16G-H, O-P). B40D and B40ED show maximum high precipitation values along the Louisiana coast and are especially centered around DWH and buoy 42040 for B40ED (Figures 4.16H). Additionally, there is a location along the Mississippi-Alabama border of consistently low experimental precipitation values in the accumulated precipitation figures (Figures 4.16 G-H, O-P) indicated by the arrows labeled “4.” Compared to NOAA’s Advanced Hydrologic Prediction Service’s (AHPS) monthly departure from normal, this location roughly matches where there are significantly low departures from normal in June and July (Figure 4.17), and this seems a reasonable comparison as most of the models’ precipitation occurs in June and July. While none of these models capture the precipitation accurately the common elements across each of them help bolster the results depicted in B40C as well as help determine some of B40C’s biases for precipitation location.

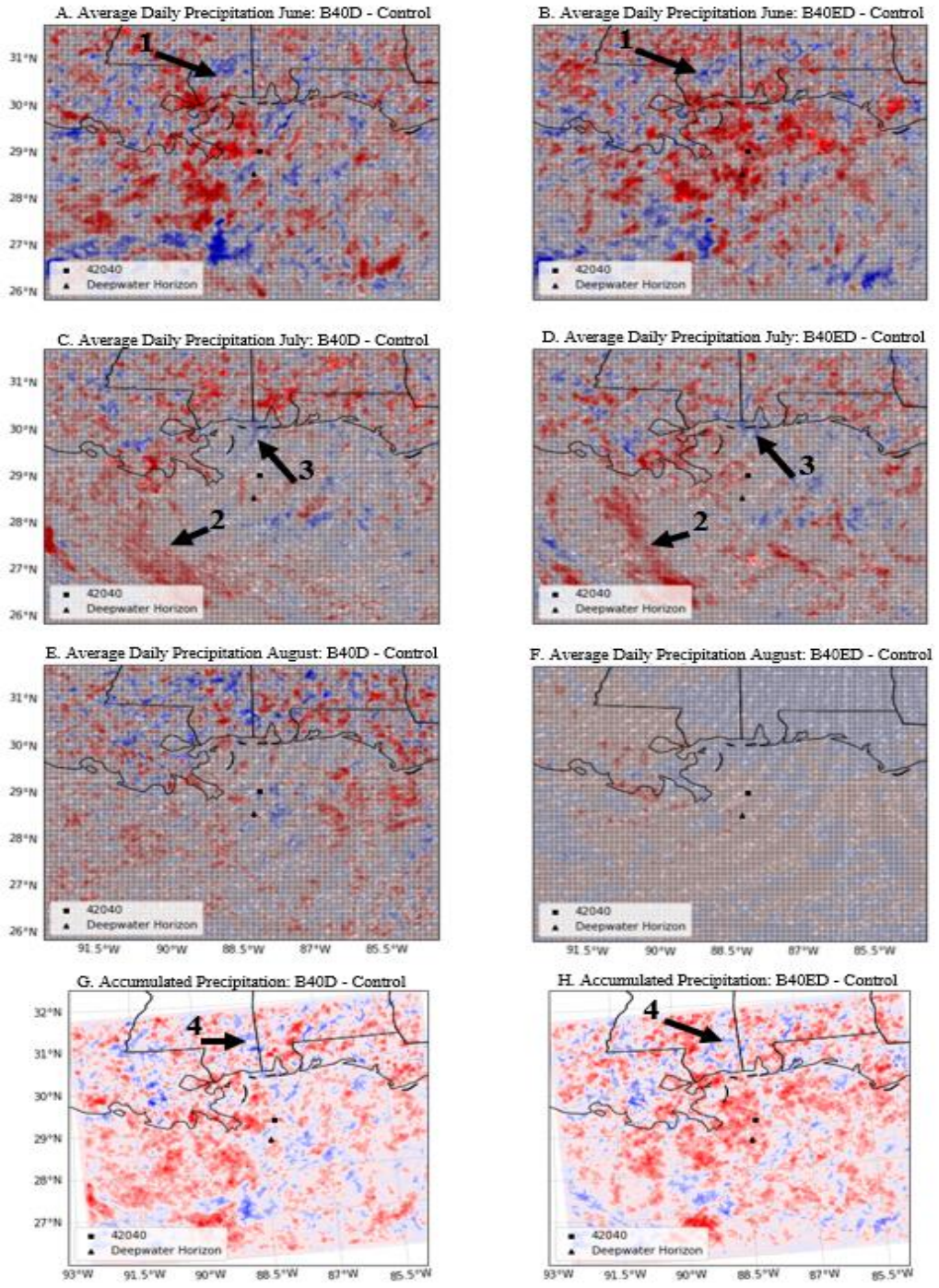

Figure 4.16. A-L) June, July, and August daily mean precipitation differences for experimental models minus the control where blue values indicate higher control precipitation and red indicates higher experimental precipitation. Stippled areas indicate statistical insignificance with a 95% confidence. M-P) Accumulated precipitation differences between B40D, B40ED, and A40D minus the control. Q) Oil slick footprint outline. The black arrows indicate areas of interest.

Figure Continued.

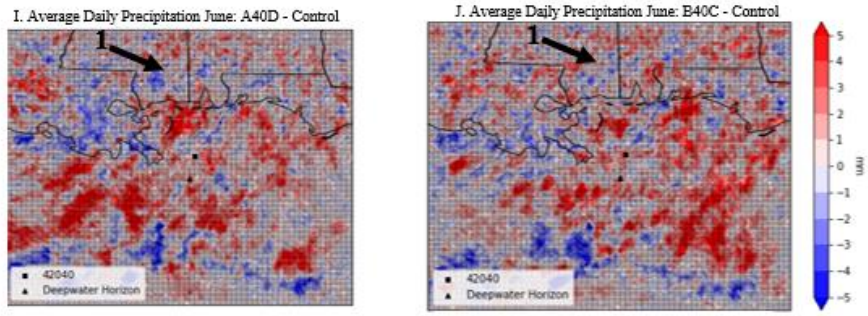
I. Average Daily Precipitation June: A40D - Control
J. Average Daily Precipitation June: B40C - Control
1
1
42040
Deepwater Horizon
42040
Deepwater Horizon
mm
5
4
3
2
1
0
−1
−2
−3
−4
−5

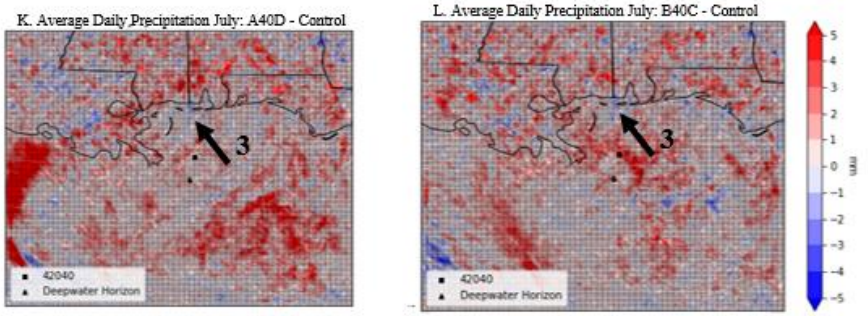
K. Average Daily Precipitation July: A40D - Control
L. Average Daily Precipitation July: B40C - Control
3
3
42040
Deepwater Horizon
42040
Deepwater Horizon
mm
5
4
3
2
1
0
−1
−2
−3
−4
−5

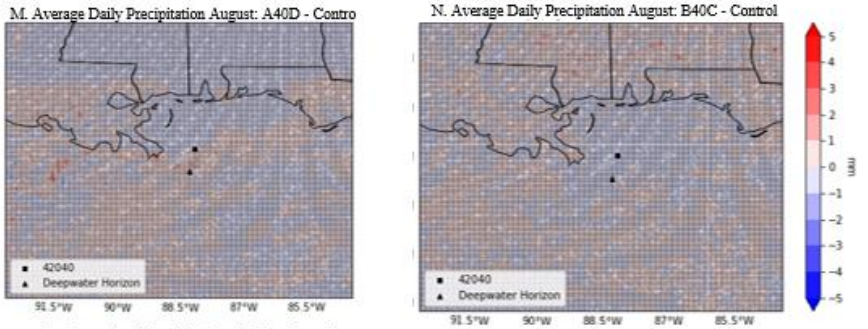
M. Average Daily Precipitation August: A40D - Contro
N. Average Daily Precipitation August: B40C - Control
42040
Deepwater Horizon
42040
Deepwater Horizon
91.5°W
90°W
88.5°W
87°W
85.5°W
mm
5
4
3
2
1
0
−1
−2
−3
−4
−5

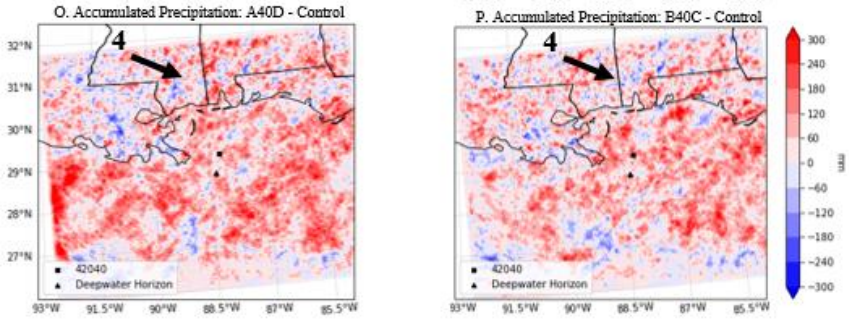
O. Accumulated Precipitation: A40D - Control
P. Accumulated Precipitation: B40C - Control
4
4
32°N
31°N
30°N
29°N
28°N
27°N
42040
Deepwater Horizon
42040
Deepwater Horizon
93°W
91.5°W
90°W
88.5°W
87°W
85.5°W
mm
300
240
180
120
60
0
−60
−120
−180
−240
−300

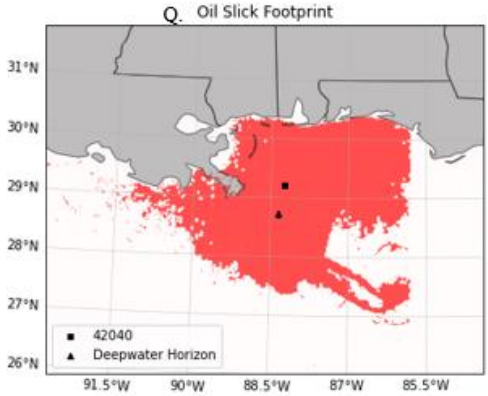
Q. Oil Slick Footprint
31°N
30°N
29°N
28°N
27°N
26°N
42040
Deepwater Horizon
91.5°W
90°W
88.5°W
87°W
85.5°W

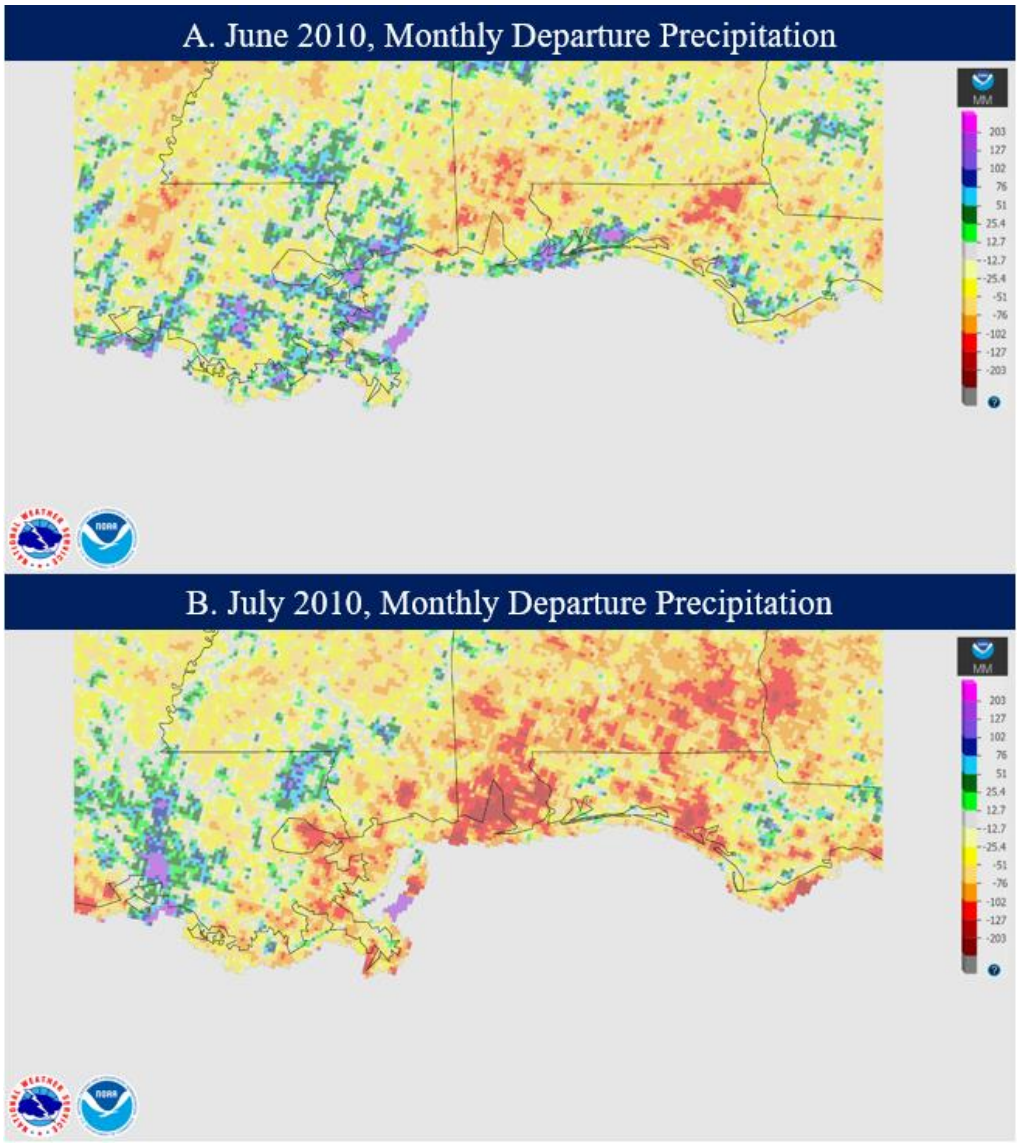

Figure 4.17. Monthly precipitation departure (mm) from normal for A) June and B) July 2010 (Taken from NOAA's AHPS website, NOAA 2023).

Chapter 5. Discussion

5.1. Response in the Uniform-Increase Scenario

Because B40C closely matched the observed warming by buoy 42040 near the epicenter of the DWH spill, it will serve as the initial basis for understanding how the elevated SSTs altered meteorological variables. Logically, the elevated SSTs would in turn elevate the temperatures of the air just above the surface. This is clear in Figure 4.2 as the T2s roughly match the outline of the oil slick footprint. This increase in air temperature near the surface causes an increase in the kinetic energy of air particles which then would increase the volume of this imaginary air parcel. The increase in space for the air particles within this parcel over the oil spill leads to a reduction of density and results in lower SLP across much of the domain (Figure 4.4). This increases in June and July when the elevated footprint SSTs were at their highest. The most outstanding features during July were the large swath of cooler B40C T2s and TD2s in the southwestern corner of the domain and the increase in both variables over the rough outline of the slick footprint (Figures 4.2 and 4.3). Additionally, as seen in the SLPs for July (Figure 4.4C), the difference values are closer to zero along the same swath mentioned, likely a result of the previously mentioned elevated T2s creating a localized zone of lower surface pressure over the slick footprint and a residual zone of relatively high pressure outside of it. As the maximum regions of lower SLP for both June and July were along the Alabama-Florida coastline (Figure 4.5), it follows that B40C's wind speeds show higher values near the coastline. A combined result from the aforementioned variables shows that in July B40C has a smaller amount of low-level cloud fraction coverage along the southwestern quadrant of the domain (Figure 4.7D), consistent with the greater dew point depression for B40C over that region. B40C has greater

fractions of mid and high-level clouds as seen in Figures 4.7E and 4.7D as well as higher LCL heights in July for B40C (Figure 4.8).

During July, over the oil footprint, and along the Florida coastline there was a greater amount of low-level cloud generation occurring in B40C (Figures 4.7D and 4.8). Simultaneously, the TD2s were at their highest near Florida and elevated SSTs were still strong, so the extra moisture and heat (Figures 4.2C and 4.3C) linked to the warmer SSTs could be driving additional cloud coverage in these areas. Cloud fractions in June are greater in the control model compared to B40C (Figures 4.7A-C), especially along the Louisiana-Mississippi-Alabama coastline. This is most likely due to the lower experimental TD2s over this same area while having roughly equal levels of T2s thereby rendering a larger dew point depression and a dryer column of air. The greater moisture and cloud coverage over the central-eastern GOM then translates to greater precipitation seen in Figure 4.9B. The model precipitation was maximized in June with some additional rainfall coming in July (Figure 4.10); B40C had little difference from the control in August, however, consistent with the gradual reduction in B40C's SSTs elevation towards the end of the spill. Over the course of the simulation, as the SSTs increased over the oil slick and subsequently increasing the T2s, the resulting lower pressure and increased moisture allowed a greater quantity of precipitation to resolve over and surrounding the footprint seen by B40C placing precipitation more accurately and more successfully within the GOM than the control.

5.2. Response in Decay Models

Each of the decay scenarios largely follows the same trend set by B40C. Each features an elevation in T2s corresponding with the elevation in SSTs per scenario, but compared to the large, uniform increase in SSTs in B40C, the effects from the decay models were more localized

around the maximum frequency portions of the oil slick footprint (Figure 4.11). B40ED shows the highest changes in T2s followed by B40D and then A40D. The decay scenarios all also showed the belt of lower T2s in the southwest quadrant of the domain in July (Figures 4.11B 4.11E, and 4.11H) that corresponded to lower TD2 values in the same regions (Figures 4.12B 4.12E, and 4.12H). When examining the alterations of TD2s in July, the swath of lower decay scenario TD2s is not as well formed as in B40C. B40D and B40ED both feature lower SLPs along the entire coastline, but for B40ED, the higher SST elevation seems to have created a similar spatial scale as B40C except B40ED's maximum low pressure was centered over the highest raised SSTs near DWH (Figure 4.13E). Wind speed for the decay models also resembles the B40C scenario. In June and July, there are regions of slower decay model wind speeds along the coastline of Mississippi and Alabama as well as faster wind speeds over the oil slick footprint (Figure 4.14), following the hypothesized effects on the sea breeze; however, because WRF was configured to output conditions at six hourly time steps, viewing the land breeze and sea breeze cycle was inconclusive. The alterations of SSTs in the decay scenarios compared to B40C altered slightly the cloud fraction distribution seen in July in Figure 4.15. Where B40C and A40D had a wide cloud fraction covering much of the central-eastern domain in the middle and high-levels, B40D and B40ED had a more concentrated swath from the northwest corner down to the southeast (Figures 4.15B, 4.15E, 4.15H, and 4.15K). This is most likely a result of B40Cs more expansive SST increase versus the more concentrated SST increase in B40D and B40ED; however, A40D fails to confirm this pattern, which would be expected to appear similar to the other decay scenarios.

High dew point depressions in June and July over the Mississippi-Alabama border (Figures 4.11 and 4.12) stood out in B40C and B40ED, as well as the other decay models but to a

lesser degree. This seems to correspond to the lower levels of precipitation generated in each scenario just north of this region in Figure 4.16 indicated by the arrows labeled “1”, “3”, and “4” which also matches up with the June precipitation for B40C (figures 4.16D, H, L, and P). Each of these decay scenarios also resulted in higher quantities of precipitation occurring over the offshore portion of the domain compared to the control. The degree to which the decay scenario was elevated seems to play an important role in determining where the increased precipitation will occur (Figure 4.16M-P). B40ED places most of the precipitation near the central area of the domain whereas B40D places it farther west. A40D is the model that stands out the most because it shows the highest precipitation across the domain ocean compared to the other experimental models. The rest of the models increase in precipitation quantity and area with the increase in SST elevation and frequency, and while A40D still largely exhibits the same spatial precipitation patterns, the total varies tremendously (Figure 4.16O). Despite variances between the models, the chain of events leading from the SSTs increasing, to the increase in T2s and TD2s, followed by a decrease in SLP altering the wind gradient, and precipitation totals and locations remain somewhat consistent across the decay models and B40C.

Chapter 6. Conclusions

By persistently altering the energy exchange at the sea surface, an oil spill may influence the local meteorological conditions. The confluence of the DWH oil spill during the 2010 summer with the synoptic and mesoscale conditions resulted in a unique hydrometeorological outcome. The Bermuda High was abnormally strong and likely helped confine the oil slick along the coast. The accident had to occur early in the summer and then last long enough to add to the naturally increasing SSTs during an otherwise synoptically quiescent summertime. The existence of a large oil patch on the ocean surface for an extended duration, the increased solar radiation absorption at the sea surface is posited to have altered wind speeds, temperatures, and dew points. By the comparison of five WRF simulations spanning roughly four and a half months, there is evidence that elevated SSTs from a long-term oil slick with warm 2-m air temperatures and cool 2-m dew point temperatures, lower surface pressure, increase cloud height while increasing precipitation offshore and decreasing it in several key locations onshore. Although temperature, moisture, and wind speed differences were statistically insignificant, the fact remains that there were also many patterns between the different models and observed data despite the differences in SST perturbations. The locations where little precipitation was produced in the experimental models roughly correspond with observed locations of abnormally low rainfall. While the method of incorporating the oil slick into WRF required assumptions and approximations, the results they produced and the consistencies between models are still worthy of consideration.

The ecological and financial impacts of an oil spill on the ocean are devastating and especially along a coast where so many industries from tourism to fishing and fisheries are crucial to local communities While these result in lasting damages to the environment that are

difficult to recover in a human lifetime, the somewhat indirect method of alteration and not-directly-dangerous effects on the atmosphere and local meteorology is an area that has not been previously studied. Partially this is due to the typically small timescale of oil spill cleanup; however, with the likely continual rise in global ocean temperatures (IPCC 2022), the chances of an oil spill compounding high SSTs could increase the likelihood of slick-altered meteorological conditions. More research into this subject could help local meteorologists when predicting rainfall patterns for a coastal region or even while predicting surface wind and temperature forecasts for oil spill cleanup.

Future studies to refine the process of including oil into WRF as well as to discover further unknown effects of a major oil disaster on the atmosphere would be beneficial. Primarily, future research should create a simulation without the fading out of the elevated SSTs as it was seen in the observed precipitation data that August was the peak rainfall accumulation while the models all featured their peak precipitation in June corresponding to the SST elevation peaks. Additionally, research into the effects of seasonality on an oil spill could identify if and how a wintertime spill would affect regional meteorology. Further, analyzing a long-term oil spill on a year without such a strong Bermuda High could help identify how the synoptic scale circulation modulate the SST effects and impacts the oil. Another recommendation would be narrowing the time scale to determine the time required for an oil spill to start altering the atmospheric cycles.

Despite the hyper-specificity of this event, it is very possible to broaden this work to other locations by the fundamental physics of how the oil interacts with the atmosphere. This novel approach could open the doors to a wider body of work beyond the typically important oil research and allow a better understanding of how humanity shapes the planet.

References

Aeppli, C. (2022). Recent Advance in Understanding Photooxidation of Hydrocarbons after Oil spills. Current opinion in Chemical Engineering, 36, 100763.

Aeppli, C., Mitchell, D. A., Keyes, P., Beirne, E. C., McFarlin, K. M., Roman-Hubers, A. T., Rusyn, I., Prince, R. G., Zhao, L., Parkerton, T. F., & Nedwed, T. (2022). Oil Irradiation Experiments Document Changes in Oil Properties, Molecular Composition, and Dispersant Effectiveness Associated with Oil Photo-Oxidation. Environmental Science Technologies, 56(12), 7789–7799.

Armson, D., Stringer, P., & Ennos, A. R. (2012). The Effect of Tree Shade and Grass on Surface and Globe Temperatures in an Urban Area. Urban Forestry & Urban Greening, 11(3), 245–255.

Andreou, C., & Karathanassi, V. (2011). Endmember Detection in Marine Environment with Oil Spill Event. Image and Signal Processing for Remote Sensing XVII, 8180, 1–8.

Bornstein, R. & Lin, Q. (2000). Urban Heat Islands and Summertime Convective Thunderstorms in Atlanta: Three Case Studies. Atmospheric Environment, 34(3), 507–516.

Bothun, G. D. (2019). Ignoring Quantitative Reasoning: The Initial Estimates of the Size of the *Deepwater Horizon* Oil Spill of 2010 and the Failure of Science in Properly Shaping the Policy Response. Case Studies in the Environment, 3(1), 1–7.

Brekke, C., & Solberg, A. H. S. (2005). Oil Spill Detection by Satellite Remote Sensing. Remote Sensing of Environment, 95(1), 1–13.

Bureau of Safety and Environmental Enforcement. (2013). Spill Summaries OCS Spills ≥ 50 Barrels CY 1964 – 2013. BSEE Spills Archive. https://www.bsee.gov/sites/bsee.gov/files/reports/incident-and-investigations/spills-greater-than-50-barrels1964-2012-as-of-august-3-2012.pdf.

Camilli, R., Di Lorio, D., Bowen, A., Reddy, C. M., Techet, A. H., Yoerger, D. R., Whitcomb, L. L., Seewald, J. S., Sylva, S. P., & Fenwick, J. (2011). Proceedings of the National Academy of Sciences, 109(50), 20235–20239.

Changnon Jr., S. A., Semonin, R. G., & Huff, F. A. (1976). A Hypothesis for Urban Rainfall Anomalies. Journal of Applied Meteorology and Climatology, 15(6), 544–560.

Chun, B., & Guldmann, J.- M. (2018). Impact of Greening on the Urban Heat Island: Seasonal Variations and Mitigation Strategies. Computers, Environment, and Urban Systems, 71, 165–176.

Cochrane, J. d., & Kelly, F. J. (1986). Low-Frequency Circulation on the Texas- Louisiana Continental Shelf. Journal of Geophysical Research: Oceans, 91, 10645–10659.

Cohen, M. A. (2010). A Taxonomy of Oil Spill Costs – What Are the Likely Costs of the *Deepwater Horizon* Spill?. Resources for the Future, 1–7.

Copernicus-ECMWF. (2022). Sea Surface Temperature Daily Data from 1981 to Present Derived from Satellite Observations. Copernicus Climate Data Store. https://cds.climate.copernicus.eu/cdsapp#!/dataset/satellite-sea-surface-temperature?tab=overview.

Court, C., Hodges, A. W., Coffey, K., Ainsworth, C. H., & Yoskowitz, D. (2019). Effects of the *Deepwater Horizon* Oil Spill on Human Communities: Catch and Economic Impacts. Deep Oil Spills, 569–580.

Crone, T. J., & Tolstoy, M. (2010). Magnitude of the 2010 Gulf of Mexico Oil Leak. Science, 330(6004), 634.

Debbage, N., Miller, P., Poore, S., Morano, K., Mote, T. J., & Shepherd, J. M. (2017). A Climatology of Atmospheric River Interactions with the Southeastern United States Coastline. International Journal of Meteorology, 37(11), 4077–4091.

Deilami, K., Kamruzzaman, M, & Liu, Y. (2018). Urban Heat Island Effect: A Systematic Review of Spatio-temporal Factors, Data, Methods, and Mitigation Measures. International Journal of Applied Earth Observation and Geoinformation, 67, 30–42.

Dewan, A., Kiselev, G., & Botje, D. (2021). Diurnal and Seasonal Trends and Associated Determinants of Surface Urban Heat Islands in Large Bangladesh Cities. Applied Geography, 135, 102533.

Doerry, A. W., & Dickey, F. M. (2004). Synthetic Aperture Radar. Optics and Photonics News, 15(11), 28–33.

Dyer, J. L., & Rigby, J. R. (2020) Assessing the Sensitivity of Lower Atmospheric Characteristics to Agricultural Land use Classification over the Lower Mississippi River Aluvial Valley. *Theoretical Applied Climatology*, 142, 305–320.

Emery, W. J., Castro, S., Wick, G. A., Schluessel, P., & Donlon, C. (2001). Estimating Sea Surface Temperature from Infrared Satellite and In Situ Temperature Data. Bulletin of the American Meteorological Society, 82(12), 2773–2786.

Environmental Protection Agency Office of Emergency and Remedial Response. (YEAR?) The Behavior and Effects of Oil Spills in Aquatic Environments. US EPA Archive Document. https://archive.epa.gov/emergencies/docs/oil/edu/web/pdf/chap1.pdf.

Environmental Response Management Application Gulf of Mexico. (YEAR?) Cumulative TCNNA SAR Oiling – Days of Oiling (PDARP). Created December 31, 2016. https://erma.noaa.gov/gulfofmexico#/layers=3+28400+38336&x=-88.56836&y=28.66048&z=7.2&view=2795&panel=layer.

Espedal, H. (1999). Detection of Oil Spill and Natural Film in the Marine Environment by Spaceborne SAR. IEEE 1999 International Geoscience and Remote Sensing Symposium, 3, 1478–1480.

Fingas, M. F., & Brown, C. E. (1997). Review of Oil Spill Remote Sensing. Marine Pollution Bulletin, 83(4), 199–208.

Fingas, M. F., & Brown, C. E. (2013). Oil Spill Remote Sensing. Earth System Monitoring, 337–388.

Fingas, M. F., & Brown, C. E. (2014). Review of Oil spill Remote Sensing. Marine Pollution Bulletin, 83(1), 9–23.

Fingas, M.F., & Brown, C. E. (2017). A Review of Oil Spill Remote Sensing, 18(1), 1–18. 91–109.

Frey, R. A., Ackerman, S. A., Liu, Y., Strabala, K. I., Zhang, H., Key, J. R., & Wang, X. (2008). Cloud Detection with MODIS. Part I: Improvements in the MODIS Cloud Mask for Collection 5. Journal of Atmospheric and Oceanic Technology, 25(7), 1057–1072.

Gade, M., Alpers, W., Hühnerfuss, H., Wismann, V. R., & Lange, P. A. (1998). On the Reduction of the Radar Backscatter by Oceanic Surface Films: Scatterometer Measurements and Their Theoretical Interpretation. Remote Sensing of Environment, 66(1), 52–70.

Good, W. S., Warden, R., Kaptchen, P. F., Finch, T., Emery, W. J., & Giacomini, A. (2011). Absolute Airborne Thermal SST measurements and Satellite Data Analysis from the *Deepwater Horizon* Oil Spill. Monitoring and Modeling the *Deepwater Horizon* Oil Spill: A Record-Breaking Enterprise, 195.

Goodman, R. (1994). Overview and Future Trends in Oil Spill Remote Sensing. Science & Technology Bulletin, 1(1), 11–21.

Grüner, K., Reuter, R., & Smid, H. (1991). A New Sensor System for airborne Measurements of Maritime Pollution and of Hydrographic Parameters. GeoJournal, 24, 103–117.

Gullet, B. K., Hays, M. D., Tabor, D., & Vander Wal, R. (2016). Characterization of the Particulate Emissions from the BP *Deepwater Horizon* Surface Oil Burns. Marine Pollution Bulletin, 107(1), 216–223.

Gullet, B. K., Aurell, J., Holder, A., Mitchel, W., Greenwell, D., Hays, M., Commy, R., Tabor, D., Preston, W., George, I., Abrahamson, J. P., Vander Wal, R., & Holder, E. (2017). Characterization of Emissions and Residues from Simulations of the *Deepwater Horizon* Surface Oil Burns. Marine Pollution Bulletin, 117(1–2), 392–405.

Gutro, R. (2010). Hurricane Season 2010: Tropical Depression 2 (Gulf of Mexico). National Aeronautics and Space Administration Hurricanes/Tropical Cyclones. https://www.nasa.gov/mission_pages/hurricanes/archives/2010/h2010_02.html.

Haines, S. L., Jedlovec, G. J., & Lazarus, S. M. (2007). A MODIS Sea Surface Temperature Composite for Regional Applications. IEEE Transactions on Geoscience and Remote Sensing, 45(9), 2919–2927.

Han, J. Y., Baik, J. J., & Lee, H. (2014). Urban Impacts on Precipitation. Asia-Pacific Journal of Atmospheric Sciences, 50, 17–30.

Hersbach, H., Bell, B., Berrisford, P., Hirahara, S., Horányi, A., Muñoz-Sabater, J., ... & Thépaut, J. N. (2020). The ERA5 Global Reanalysis. Quarterly Journal of the Royal Meteorological Society, 146(730), 1999–2049.

Hjelmfelt, M. R. (1982). Numerical Simulation of the Effects of St. Louis on Mesoscale Boundary-Layer Airflow and Vertical Air Motion: Simulations of Urban vs. Non-urban Effects. Journal of Applied Meteorology, 21(9), 1239–1257.

Huffman, G. J., Bolvin, D. T., Braithwaite, D., Hsu, K., Joyce, R., Xie, P., & Yoo, S. H. (2015). NASA Global Precipitation Measurement (GPM) Integrated Multi-satellite Retrievals for GPM (IMERG). *Algorithm Theoretical Basis Document (ATBD) version,* 4(26).

Hui-yan, S., Pu-cheng, Z., & Shao-ru, F. (2011). Research on Multi-angle near Infrared Spectral-Polarimetric Characteristic or Polluted Water by Spilled Oil. International Symposium on Photoelectric Detection and Imaging 2011: Advances in Infrared Imaging and Applications, 8193, 175–180.

Imhoff, M. L., Zhang, P., Wolfe, R. E., & Bounoua, L. (2010). Remote Sensing of the Urban Heat Island Effect across Biomes in the Continental USA. Remote Sensing of Environment, 114(3), 504–513.

Innman, A., Easson, G., Asper, V. L., & Diercks, A.- R. (2010). The Effectiveness of Using MODIS Products to Map Sea Surface Oil. Oceans 2010 MTS/IEE Seattle, 1–5.

Begum, A. R., Lempert, R., Ali, E., Benjaminsen, T. A., Bernauer, T., Camer, W., Cui, X., Mach, K., Nagy, G., Stenseth, N. C., Sukumar, R., & Wester, P. (2022). Contribution of Working Group II to the Sixth Assessment Report of the Intergovernmental Panel on Climate Change. Point of Departure and Key Concepts. Climate Change 2022: Impacts, Adaptation, and Vulnerability [Pörtner, H.-O., Roberts, D. C., Tignor, M., Poloczanska E. S., Mintenbeck, K., Alegria, A., Craig, M., Langsdorf, S., Löschke, S., Möller, V., Okem, A., & Rama, B. (eds)].

Jacobi, M., Kinner, N. E., Braswell, B. H., Schwehr, K. D., Newman, K. S., Merten, A. A. (2008). Environmental Response Management Application. International Oil Spill Conference Proceedings 1 May 2008, 2008(1), 881–885.

Jha, M. N., Levy, J., & Gao, Y. (2008). Advances in Remote Sensing for Oil Spill Disaster Management: State-of-the-Art Sensors Technology for Oil Spill Surveillance. Sensors for Disaster and Emergency Management Decision Making, 8(1), 236–255.

Jones, B. (2001). A Comparison of Visual Observations of Surface Oil with Synthetic Aperture Radar Imagery of the Sea Empress Oil Spill. International Journal of Remote Sensing, 22(9), 1619–1638.

Joye, S. B. (2015). *Deepwater Horizon*, 5 Years on. Science, 349(6248), 592–593.

Legeckis, R. V. (1979). Satellite Observations of the Influence of Bottom Topography on the Seaward Deflection of the Gulf Stream off Charleston, South Carolina. Journal of Physical Oceanography, 9(3), 483–497.

MacDonald, I. (2010). Deepwater Disaster: How the Oil Spill Estimates Got It Wrong. Significance, 7(4), 149–154.

MacDonald, I. R., Garcia-Pineda, O., Beet, A., Daneshgar Asl, S., Feng, L., Graettinger, G., French-McCay, D., Holmes, J., Hu, C., Huffer, F., Leifer, I., Muller-Karger, F., Solo, A., Silva, M., & Swayze, G. (2015). Natural and Unnatural Oil Slicks in the Gulf of Mexico. Journal of Geophysical Research: Oceans, 120(12), 8364–8380.

Manley, G. (1958). On the Frequency of Snowfall in Metropolitan England. Quarterly Journal of the Royal Meteorological Society, 84(359), 70–72.

McClain, E. P., Pichel, W. G., & Walton, C. C. (1985). Comparative Performance of AVHRR-Based Multichannel Sea Surface Temperatures. Journal of Geophysical Research, 90(C6), 11587–11601.

McNutt, M. K., Camilli, R., Crone, T. J., Guthrie, G. D., Hsieh, P. A., Ryerson, T. B., Savas, O., & Shaffer, F. (2012). Review of Flow Rate Estimates of the *Deepwater Horizon* Oil Spill. Proceedings of the National Academy of Sciences, 109(50), 20260–20267.

Merchant, C. J., Embury, O., Bulgin, C. E., Block, T., Corlett, G. K., Fiedler, E., Good, S. A., Mittaz, J., Rayner, N. A., Berry, D., Eastwood, S., Taylor, M., Tsushima, Y., Waterfall, A., Wilson, R., & Donlon, C. (2019). Satellite-Based Time-Series of Sea-Surface Temperature Since 1981 for Climate Applications. Scientific Data, 6(223), 1–18.

Miller, P. W., & Mote, T. L. (2017). A Climatology of Weakly Forced and Pulse Thunderstorms in the Southeast United States. Journal of Applied Meteorology and Climatology, 56(11), 3017–3033.

Miller, P.W., Mote, T. L., Kumar, A., & Mishra, D. R. (2019). Systematic precipitation redistribution following a strong hurricane landfall. *Theoretical Applied Climatology*, 139, 861–872.

Miller, P. (2022a). Oil Influence on Sea Breezes. Personal Communication

Miller, P. (2022b). Radar Reflectivity on 2010-06-15. Personal Communication

Minnet, P. J., Alvera-Azcárate, A., Chin, T. M., Corlett, G. K., Gentermann, C. L., Karagali, I., Li, X., Marsouin, A., Marullo, S., Maturi, E., Santoleri, R., Picart, S. S., Steele, M., & Vazquez-Cuervo, J. (2019). Half a Century of Satellite Remote Sensing of Sea Surface Temperature. Remote Sensing of Environment, 233, 111366.

NOAA CoastWatch. (2022). AVHRR Sea Surface Temperature. NOAA CoastWatch East Coast Node. https://eastcoast.coastwatch.noaa.gov/cw_avhrr.php.

NOAA National Centers for Environmental Information, Sate of the Climate: Monthly National Climate Report for Annual 2010. Published online January 2011. Retrieved from https://www.ncei.noaa.gov/access/monitoring/monthly-report/national/201013.

NOAA. (2023). Monthly Departures from Normal Precipitation for June 2010. NOAA AHPS. https://water.weather.gov/precip/.

NWS Hurricane Alex, June 30 – July 2, 2010. National Weather Service, Corpus Cristi, Texas. https://www.weather.gov/crp/hurricanealex.

Nodvik, A. B. (1999). Time Window-of-Opportunity Strategies for Oil Spill Planning and Response. Pure and Applied Chemistry, 71(1), 5–16.

Oil Tanker Spill Statistics 2021 (2021). International Tanker Owners Pollution Federation Limited. https://www.itopf.org/knowledge-resources/data-statistics/statistics/.

Olascoaga, M. J., & Haller, G. (2012). Forecasting Sudden Changes in Environmental Pollution Patterns. Proceedings of the National Academy of Sciences, 109(13), 4738–4743.

Perring, A. E., Scharz, J. P., Spackman, J. R., Bahreini, R., de Gouw, J. A., Gao, R. S., Holloway, J. s., Lack, D. A., Langridge, J. M., Peischl, J., Middlebrook, A. M., Ryerson, T. B., Warneke, C., Watts, L. A., & Fahey, D. W. (2011). Characteristics of Black Carbon Aerosol from a Surface Oil Burning during the *Deepwater Horizon* Oil Spill. Geophysical Research Letters, 38, L17809.

Pinto, O., Pinto, I. R. C. A., & Neto, O. P. (2013). Lightning Enhancement in the Amazon Region Due to Urban Activity. American Journal of Climate Change, 2(4), 270–274.

Price, J. C. (1979). Assessment of the Urban Heat Island Effect through the Use of Satellite Data. Monthly Weather Review, 107(11), 1554–1557.

Román-Cascón, C., Mulero-Martínez, R., Bruno, M., Yagüe, C., Lothon, M., Lohou, F., ... & Adame, J. A. (2021). How do the Sea and the Land Conditions Affect the Coastal Breezes? 20 Days Analysed from WRF Simulations in the Gulf of Cadiz (Iberian Peninsula) (No. EMS2021-344). Copernicus Meetings.

Rudich, Y., Sagi, a., Rosenfeld, D. (2003). Influence of the Kuwait Oil Fires Plume (1991) on the Microphysical Development of Clouds. Journal of Geophysical Research-Atmospheres, 108(D15), L4478.

Ryerson, T. B., Camilli, R., Kessler, J. D., Kujawinski, e. B., Reddy, C. M., Valentine, D. L., Atlas, E., Blake, D. R., De Gouw, J., Meinardi, S., Parrish, D. D., Peischl, J., Seewald, J. S., & Warneke, C. (2012). Chemical Data Quantify *Deepwater Horizon* Hydrocarbon Flow Rate and Environmental Distribution. Proceedings of the National Academy of Sciences, 109(50), 20246–20253.

Salisbury, J. W., D'Aria, D. M., & Sabins, F. F. (1993). Thermal Infrared Remote Sensing of Crude Oil Slicks. Remote Sensing of Environment, 45(2), 225–231.

Samberg, A. (2005). Advanced Oil Pollution Detection Using an Airborne Hyperspectral Lidar Technology. Laser Radar Technology and Applications X, 5791, 308–317.

Samra, R. M. A., El-Gammal, M., & Eissa, R. (2021). Oceanographic Factors of Oil Pollution dispersion Offshore the Nile Delta (Egypt) Using GIS. Environmental Science and Pollution Research, 28, 25830–25843.

Shen, H. Y., Zhou, P. C., Feng, S. R. (2011). Research on Multi-angle Near Infrared Spectral-polarimetric Characteristic for Polluted Water by Spilled Oil. International Symposium on Photoelectronic Detection and Imaging 2011, 8193, 81930M-1-81930M-6.

Shepherd, J. M., Stallins, J. A., Jin, M. L., & Mote, T. L. (2010). Urbanization: Impacts on Clouds, Precipitation, and Lightning. Urban Ecosystem Ecology, 55, 1–28.

Skamarock, W. C., Klemp, J. B., Dudhia, J., Gill, D. O., Liu, Z., Berner, J., Wang, W., Powers, J. G., Duda, M. G., Barker, D. M., & Huang, X. (2019). A Description of the Advanced Research WRF Model Version 4. *National Center for Atmospheric Research: Boundler, CO, USA*, 145(145), 550.

Srivastava, A. K., Ulrich, P. A., Rastogi, D., Vahmani, P., Jones, A., & Grotjahn, R. (2023). Assessment of WRF (v 4.2.1) Dynamically Downscaled Precipitation on Subdaily and Daily Timescales over CONUS. EGUsphere[preprint]

Stahle, D. W., & Cleaveland, M. K. (1996). Large-scale Climatic Influences on Baldcypress Tree Growth across the Southeastern United States. In: Jones, P.D., Bradley, R. S., Jouzel, J. (eds) Climatic Variations and Forcing Mechanisms of the Last 2000 Years. NATO ASI Series, 41.

Stallins, J. A., & Rose, L. S. (2008). Urban Lighting: Current Research, Methods, and the Geographical Perspective. Geography Compass, 2(3), 620–639.

Stone, B., & Rodgers, M. O. (2001). Urban Form and Thermal Energy. Journal of the American Planning Association, 67(2), 186–198.

Suo, Z., Lu, Y., Liu, J., Ding, J., Yin, D., Xu, F., & Jiao, J. (2021). Ultraviolet Remote Sensing of Marine Oil Spills: A New Approach of Haiyang-1C Satellite. Optics Express, 29(9), 13486–13495.

Taft, D. G., Egging, D. E., & Kuhn, H. A. (1995). Sheen Surveillance: An Environmental Monitoring Program Subsequent to the 1989 Exxon Valdez Shoreline Cleanup. Exxon Valdez Oil Spill: Fate and Effects in Alaskan Waters, 215–239.

Tseng, W. Y., & Chiu, L. S. (1994). AVHRR Observations of Persian Gulf Oil Spills. Proceedings of IGARSS ’94 – 1994 IEEE International Geoscience and Remote Sensing Symposium, 2, 779–782.

Tyo, J. S., Goldstein, D. L., Chenault, D. B., & Shaw, J. A. (2006). Review of Passive Imaging Polarimetry for Remote Sensing Applications. Applied Optics, 45(22), 5453–5469.

National Data Buoy Center (1971). Meteorological and Oceanographic Data Collected from the National Data Buoy Center Coastal-Marine Automated Network (C-MAN) and moored (weather) Buoys. https://www.ndbc.noaa.gov/.

Ward, C. P., Reddy, C. M., & Overton, E. B. (2020). Why Sunlight Matters for Marine Oil Spills. EOS, 101.

Walker, N. D., Rouse, L. J., Fargion, G. S., & Biggs, D. C. (1994). The Great Flood of Summer 1993: Mississippi River Discharge Studied. EOS Transactions, American Geophysical Union, 75(36), 409–415.

Walker, N. D., Wiseman Jr., W. J., Rouse Jr., L. J., & Babin, A. (2005). Effects of River Discharge, Wind Stress, and Slope Eddies on Circulation and the Satellite-Observed Structure of the Mississippi River Plume.

Walker, N. D., Pilley, C. T., Raghunathan, V. V., D'Sa, E. J., Leben, R. R., Hoffmann, N. G., Brickley, P. J., Coholan, P. D., Sharma, N., Graber, H. C., Turner, R. E. (2011). Impacts of Loop Current Frontal Cyclonic Eddies and Wind Forcing on the 2010 Gulf of Mexico Oil Spill. Monitoring and Modeling the Deepwater Horizon Oil spill: A Record-Breaking Enterprise, Geophysical Monograph Series 195, American Geophysical Union, 103–116.

Williams, E. R. (1994). Global Circuit Response to Seasonal Variations in Global Surface Air Temperature. Monthly Weather Review, 122(8),1917–1929.

Wismann, V., Gade, M., Alpers, W., & Hühnerfuss, H. (1998). Radar Signatures of Marine Mineral Oil Spills Measured by an Airborne Multi-frequency Radar. International Journal of Remote Sensing, 19(18), 3607–3623.

Xing, Q., Li, L., Lou, M., Bing, L., Zhao, R., & Li, Z. (2015). Observation of Oil Spills through Landsat Thermal Infrared Imagery: A Case of *Deepwater Horizon*. Aquatic Procedia, 3, 151–156.

Xue, Y., Li, Y., Guang, J., Zhang, X., & Guo, J. (2008). Small Satellite Remote Sensing and Applications – History, Current and Future. International Journal of Remote Sensing, 29(15), 4339–4372.

Yang, C. S., Kim, Y. S., Ouchi, K., & Na, J. H. (2009). Comparison with L-, C-, and X-band Real SAR Images and Simulation SAR Images of Spilled Oil on Sea Surface. 2009 IEEE International Geoscience and Remote Sensing Symposium, 673–676.

Ying, L., Guo-Xin, L., Ji-Jun, L., & Long, M. (2009). Potential Analysis of Maritime Oil Spill Monitoring Based on MODIS Thermal Infrared Data. 2009 IEEE International Geoscience and Remote Sensing Symposium, 373–376.

Ylitalo, G. M., Krahn, M. M., Dickhoff, W. W., Stein, J. E., Walker, C. C., Lassitter, C. L., Garrett, e. S., Desfosse, L. L., Mitchell, K. M., Noble, B. T., Wilson, S., Beck, N. B., Benner, R. A., Koufopoulos, P. N., & Dickey, R. W. (2012). Federal Seafood Safety Response to the *Deepwater Horizon* Oil Spill. Proceedings of the National Academy of Sciences, 109(50), 20274–20279.

Zhou, J., Chen, Y., Zhang, X., & Zhan, W. (2013). Modeling the Diurnal Variations of Urban Heat Islands with Multi-source Satellite Data. International Journal of Remote Sensing, 34(21), 7568–7588.

Vita

Charles Philip Johnson was born in Brighton, Colorado, and graduated high school in 2016 from Tupelo Mississippi High School. Attending Mississippi State University, he attained a Bachelor of Science in Operational Meteorology in 2020. In June 2021, he joined the Costal Meteorology (COMET) Laboratory under Paul Miller at Louisiana State University (LSU) and began a Master of Science in Oceanography and Coastal Sciences in August 2021. Much of his work during his time in the COMET Lab has been focused on utilizing the Weather Research and Forecasting (WRF) Model to simulate land-surface alterations for several projects. He expects to receive his degree from LSU in summer 2023.